Article:
Atkins, AL, Shaw, S and Peacock, CL (2014) Nucleation and growth of todorokite from birnessite: Implications for trace-metal cycling in marine sediments. Geochimica et Cosmochimica Acta, 144. 109 - 125. ISSN 0016-7037

https://doi.org/10.1016/j.gca.2014.08.014

Nucleation and growth of todorokite from birnessite: Implications for trace-metal cycling in marine sediments

Amy L. Atkins[1], Samuel Shaw[2] and Caroline L. Peacock[1]*

[1]University of Leeds, School of Earth and Environment, Leeds, LS2 9JT, UK.
[2]University of Manchester, School of Earth, Atmospheric and Environmental Sciences, Manchester, M13 9PL, UK.

Submitted to Geochimica et Cosmochimica Acta
4th April 2014
Revised version submitted 7th August 2014

*Corresponding author e-mail: C.L.Peacock@leeds.ac.uk

ABSTRACT

The phyllomanganate birnessite is the main Mn-bearing phase in oxic marine sediments, and through coupled sorption and redox exerts a strong control on the oceanic concentration of micronutrient trace metals. However, under diagenesis and mild hydrothermal conditions, birnessite undergoes transformation to the tectomanganate todorokite. The mechanistic details of this transformation are important for the speciation and mobility of metals sequestered by birnessite, and are necessary in order to quantify the role of marine sediments in global trace element cycles. Here we transform a synthetic, poorly crystalline, hexagonal birnessite, analogous to marine birnessite, into todorokite under a mild reflux procedure, developed to mimic marine diagenesis and mild hydrothermal conditions. We characterize our birnessite and reflux products as a time series, employing X-ray diffraction (XRD), Fourier transform infrared spectroscopy (FTIR), BET surface area analysis, scanning electron microscopy (SEM), high-resolution transmission electron microscopy (HR-TEM) and extended X-ray absorption fine structure spectroscopy (EXAFS). We provide new insight into the crystallization pathway and mechanism of todorokite formation from birnessite under conditions analogous to those found in marine diagenetic and hydrothermal settings. Specifically we propose a new four-stage process for the transformation of birnessite to todorokite, beginning with todorokite nucleation, then crystal growth from solution to form todorokite primary particles, followed by their self-assembly and oriented growth via oriented attachment to form crystalline todorokite laths, culminating in traditional crystal ripening. We suggest that, contrary to current understanding, trace metals like Ni might retard the transformation of birnessite to todorokite and be released to marine sedimentary pore-waters during this diagenetic process, thus potentially providing a benthic flux of these micronutrients to seawater.

KEYWORDS: Mn oxide; vernadite; birnessite; buserite; todorokite; oriented attachment; self-assembly; diagenesis; marine sediments.

1. INTRODUCTION

Manganese oxides are ubiquitous in oxic marine sediments and play a fundamental role in the biogeochemical cycling of trace elements in the ocean (e.g., Goldberg, 1954; Cronan, 1976; Burns and Burns, 1979; Post, 1999; Peacock and Sherman, 2007a; Sherman and Peacock, 2010; Spiro et al., 2010). Specifically, in addition to their ubiquity, they have large surface areas and are highly reactive, and so through coupled sorption and redox reactions are able to exert a strong control on the speciation, mobility and bioavailability of trace metals and micronutrients (e.g., Post, 1999).

In oxic marine sediments the main Mn-bearing phases are birnessite, buserite and todorokite (e.g., Burns and Burns, 1977). These minerals are all mixed Mn(III/IV) oxides, but birnessite and buserite are phyllomanganates (layer-type), consisting of sheets (layers) of edge-sharing MnO_6 octahedra, whereas todorokite is a tectomanganate (tunnel-type), consisting of triple chains of edge-sharing MnO_6 octahedra that share corners to form 3D tunnels. In birnessite and buserite, individual phyllomanganate sheets are stacked and separated by a hydrated interlayer region, which is partially filled with water molecules and a variety of cations to balance negative charge generated within the octahedral layers. Birnessite interlayers contain a single layer of water molecules resulting in an interlayer spacing of ~7 Å and, for example, Na^+ interlayer cations, while buserite interlayers contain a double layer of water molecules resulting in an interlayer spacing of ~10 Å and, for example, Mg^{2+} interlayer cations. In ideal todorokite, the tunnels have a square cross-section that measures three octahedra wide each side (Burns et al., 1985; Post and Bish, 1988; Post et al., 2003). In this case the tunnels equate to ~10x10 Å. In the marine environment, todorokite tunnels are typically occupied by hydrated Mg^{2+} ions (e.g., Bodeï et al., 2007), whereas in more rarely occurring terrestrial todorokites, other large cations such as Ba^{2+} are thought to concentrate in the tunnel positions (e.g., Xu et al., 2010). The 7 and 10 Å phyllomanganates often display a number of structural and physiochemical variations, most notably possessing either triclinic or hexagonal symmetry, where hexagonal symmetry results from ordered vacancies in the manganese octahedral sites (Drits et al., 1997). In addition, these minerals can also exhibit varying degrees of disorder in the stacking of the phyllomanganate sheets along the c-axis, creating a continuum between turbostratic vernadite that consists of randomly orientated sheets (where the synthetic analogue is δ-MnO_2), to c-disordered

phases that display some degree of sheet stacking, to highly crystalline phases in which sheets are ordered over several hundreds of angstroms (e.g., Villalobos et al., 2003). Natural marine birnessite is most commonly identified as a hexagonal, poorly crystalline phase, with either incoherent (vernadite) or semi-coherent (c-disordered birnessite) sheet stacking (e.g., Calvert and Price, 1970; Jauhari, 1987; McKenzie, 1989; Peacock and Sherman, 2007b; Grangeon et al., 2008). Furthermore, this suite of phyllomanganates also show variations in the proportion of Mn(III)/Mn(IV) within the layers. In vernadite Mn is predominantly present in the +4 oxidation state (e.g., Villalobos et al., 2003), while c-disordered and more crystalline phases contain a higher proportion of structural Mn(III) (e.g., Villalobos et al., 2003; Livi et al., 2011).

In the natural environment Mn(III/IV) oxides are thought to form via the microbial oxidation of Mn(II) (e.g., Brouwers, 2000; Francis et al., 2001; Bargar et al., 2000, 2005; Villalobos et al., 2003; Tebo et al., 2005; Webb et al., 2005a, b; Saratovsky et al., 2006; Spiro et al., 2010). However, although todorokite is often found intimitely associated with vernadite and both 7 and 10 Å semi-coherently stacked phyllomanganates (here collectively termed poorly crystalline phyllomanganates) in marine ferromanganese precipitates (e.g., Burns and Burns, 1978a, b; Siegel and Turner, 1983; Usui and Terashima, 1997; Banerjee et al., 1999; Bodeï et al., 2007; Peacock and Moon, 2012) it is thought to only form during the transformation of a 10 Å phyllomanganate under diagenetic and low temperature hydrothermal conditions (e.g., Burns and Burns, 1978b). Accordingly, marine ferromanganese precipitates that have precipitated directly from the water column (hydrogenetic) are typically rich in poorly crystalline phyllomanganates, those that have precipitated at the sediment-seawater interface (diagenetic) contain both poorly crystalline phyllomanganates and todorokite in variable proportions reflecting the influence of sediment pore-waters on individual precipitates, while those that have precipitated below the sediment-seawater interface in close proximity to hydrothermal fluids are generally todorokite rich (e.g., Burns and Burns, 1977).

Despite the close association of poorly crystalline phyllomanganates and todorokite in natural marine precipitates, the exact crystallization pathway and formation mechanism of todorokite from these minerals in natural environments is still unclear. This is due at least in part to the fact that the X-ray diffraction patterns of 10 Å phyllomanganate and todorokite overlap at key peaks, and in natural precipitates todorokite is also often poorly crystalline and typically found intermixed

with a variety of other poorly crystalline oxyhydroxides (e.g., Usui et al., 1997; Banerjee et al., 1999; Bodeï et al., 2007; Peacock and Moon, 2012). As such it can be very difficult to elucidate the detailed spectral, structural and morphological information necessary to determine precisely how poorly crystalline phyllomanganates transform into todorokite. The precise crystallization pathway and transformation mechanism are important however because the speciation, mobility and bioavailability of trace metals and micronutrients scavenged by the primary, authigenic phases will ultimately depend on whether these species are retained in the neo-formed todorokite or released back to sediment pore-waters and potentially then to seawater during the transformation. Notably, Bodeï et al. (2007) perform a range of high-resolution analyses, including X-ray diffraction, X-ray absorption spectroscopy and transmission electron microscopy, on a marine manganese concretion from hemipelagic sediments, and propose that todorokite forms in these settings via the dissolution-recrystallization of a single- to bi-layered hexagonal vernadite precursor (with an interlayer spacing equal to 7 Å) to a multi-layered and semi-coherently stacked Mg-rich vernadite intermediate (with 10 Å d-spacing), which then undergoes a topotactic transformation to todorokite.

In keeping with our knowledge of todorokite formation in the natural environment, the only known route to preparing synthetic todorokite involves the transformation of a phyllomanganate precursor, via either high temperature and pressure hydrothermal treatment (e.g., Giovanoli et al., 1975; Golden et al., 1986; Shen et al., 1993; Feng et al., 1995, 1998; Tian et al., 1997; Vileno et al., 1998; Luo et al., 1999; Malinger et al., 2004; Liu et al., 2005) or a refluxing process at atmospheric pressure, designed to better simulate todorokite formation in natural environments (Feng et al., 2004; Cui et al., 2006, 2008, 2009a). In all of the studies above, successful transformation required either an initial phyllomanganate precursor, or a phyllomanganate intermediate, possessing some degree of c-axis sheet stacking and an expanded (10 Å) interlayer region. More recently, Feng et al. (2010) synthesized a todorokite-like phase from a biogenic poorly crystalline hexagonal birnessite (most similar to δ-MnO_2), via a mild reflux procedure (atmospheric pressure, 100 ^{o}C), developed to better represent marine diagenetic and mild hydrothermal conditions while still achieving transformation on an observable time scale (investigated over 48 hr). In general agreement with Bodeï et al. (2007), Feng et al. (2010) propose that

their biogenic precursor transforms to a triclinic phyllomanganate intermediate (with 10 Å d-spacing), which then undergoes topotactic transformation to a todorokite-like product. Due to the poorly crystalline nature of the biogenic precursor, both the intermediate and the todorokite-like product are similarly poorly crystalline, which prevented a more detailed evaluation of the crystallization pathway and transformation mechanism.

Here we synthesize todorokite from a c-disordered hexagonal birnessite via a mild reflux procedure. Our birnessite precursor is analogous to marine birnessite and displays sufficient sheet stacking along the c-axis for identification of key spectral, structural and morphological features in the precursor, intermediate and transformation products. Similarly to Feng et al. (2010), our mild reflux procedure provides a reasonable representation of marine diagenetic and mild hydrothermal conditions, while still achieving transformation on an observable time scale (investigated over 4 weeks). The initial c-disordered birnessite, intermediate phyllomanganate and subsequent transformation products are extensively characterized using X-ray diffraction (XRD), Fourier transform infrared spectroscopy (FTIR), BET surface area analysis, scanning electron microscopy (SEM), high-resolution transmission electron microscopy (HR-TEM) and extended X-ray absorption fine structure spectroscopy (EXAFS). Through careful and combined analyses of our results we provide new insight into the crystallization pathway of todorokite formation from birnessite, and propose the first detailed mechanism for todorokite formation in the marine environment. We discuss the implications of our formation mechanism for the fate and mobility of trace metals and micronutrients sequestered by marine Mn oxides.

2. EXPERIMENTAL METHODS

2.1 Preparation of Hexagonal Birnessite Precursor

C-disordered hexagonal birnessite with an interlayer spacing of ~7 Å was synthesized following the method of Villalobos et al. (2003). Briefly, 320 mL of a 0.196 M $KMnO_4$ solution was added slowly to 360 mL of 0.51 M NaOH solution. Then 320 mL of a 0.366 M $MnCl_2$ solution was added slowly to the above mixture whilst stirring vigorously. The suspension was left to settle for approximately 4 hr. The supernatant was then removed and discarded. The remaining slurry was

181 subsequently centrifuged at 3200 g for 30 min. All resulting supernatants were
182 discarded. After centrifugation, the wet slurry was mixed with 800 mL of 1 M NaCl
183 and shaken for 45 min. The suspension was centrifuged and the supernatant
184 discarded. This process was repeated 4 times. For the last 1 M NaCl wash the pH was
185 adjusted to pH 8 via the drop-wise addition of 1 M NaOH and the suspension shaken
186 overnight. After centrifuging, the resulting paste was combined with Milli-Q (MQ)
187 water, shaken for 1 hr and centrifuged at 3200 g for 10 min. This MQ water wash
188 cycle was repeated 10 times, 1x for 1 hr, 8x for 0.5 hr and 1x overnight. Following
189 the final wash, the suspension was dialyzed for 3 days in 43 x 27 mm cellulose
190 dialysis tubing.
191
192 **2.2 Transformation of Hexagonal Birnessite to Todorokite**
193 C-disordered hexagonal birnessite was transformed to todorokite following a
194 method adapted from Feng et al. (2004, 2010). Approximately 45-50 g of the wet c-
195 disordered birnessite slurry was suspended in 3 L of 1 M $MgCl_2$ and stirred
196 moderately for 18 hr at room temperature. The resulting suspension was then
197 centrifuged to a wet paste. This produced an Mg-exchanged phyllomanganate
198 intermediate with an interlayer spacing of ~10 Å. This was re-suspended in
199 approximately 700 mL of 1 M $MgCl_2$ in a 1 L round bottom flask fitted with a glass
200 condenser. The suspension was stirred continuously and heated to and kept at reflux
201 (100 °C) using a combined heating mantle with magnetic stirrer. Suspension aliquots
202 (approximately 90 mL) were taken at time intervals of 3, 6, 9, 12, 24 and 48 hr. Each
203 suspension aliquot was cooled in a water bath to room temperature before
204 centrifuging at 3200 g for 10 min. Solutions were collected and the pH was measured
205 (calibrated to ±0.05 pH units with Whatman NBS grade buffers). All solid samples
206 were washed extensively in MQ water. After 72 hr the reflux was stopped and the
207 suspension was treated as above to give the final time series sample of 72 hr. All
208 samples were oven dried at 30 ^{o}C prior to analysis.
209
210 **2.3 Characterization of Precursor, Intermediate and Reflux Products**
211 Powder X-ray diffraction (XRD) patterns were collected using a Bruker D8
212 diffractometer, operating at 40kV/40mA and equipped with CuKα radiation (λ =
213 1.5418) and a LynxEye detector. Samples were analyzed over a range of 2-80 $^{o}2\theta$

214 with a 0.010 step size and step time of 155 sec. Fourier transform infrared (FTIR)
215 spectroscopy was performed on powdered samples using a Thermo Scientific iS10
216 FTIR spectrometer equipped with an attenuated total reflection (ATR) diamond
217 crystal. Each spectrum was an average of 32 scans with a resolution of 1 cm^{-1}.
218 Scanning electron microscopy (SEM) and transmission electron spectroscopy (TEM)
219 images were collected at the Leeds Electron Microscopy and Spectroscopy center in
220 the Institute for Materials Research at the University of Leeds. For imaging, finely
221 crushed powder samples were suspended in methanol and dispersed via sonication.
222 For SEM imaging, all samples were loaded onto individual aluminium stubs and left
223 to air dry. A platinum coating was applied to all samples prior to imaging which was
224 performed at 20 kV using an EI Quanta 650 FEGESEM. For TEM imaging, samples
225 were loaded onto individual holey carbon TEM grids. Imaging was performed at 200
226 kV on a Philips CM200 FEGTEM.
227 The average Mn oxidation state (AOS) of all synthesized Mn oxides was
228 determined by potentiometric titration (Ligane and Karplus, 1946; Gaillot, 2002).
229 Approximately 35 mg of finely ground mineral powder was reduced in 50 mL of a
230 previously standardized 0.02 M $(NH_4)_2Fe(SO_4)_2$ (Mohr Salt) solution. The
231 suspension was placed in an ultrasonic bath for up to 30 min to aid reduction. The
232 resulting solution was then titrated against a standardized 0.02 M $KMnO_4$ solution at
233 pH 2 to avoid the precipitation of Fe^{3+}. After this, 8 g of sodium pyrophosphate was
234 dissolved in 100 mL of MQ water and added to the previous Mn oxide solution. The
235 amount of reduced Mn^{2+} formed in the reduction step was determined by a second
236 titration against the standardized 0.02 M $KMnO_4$ solution, this time the mixture was
237 adjusted to pH 6.5-6.6 via the drop-wise addition of concentrated sulfuric acid. Due
238 to the strong color of the pyrophosphate complex, the equivalence point in this second
239 titration was determined by potentiometric titration. Potentiometric titrations were
240 undertaken using an automated titrator equipped with a combined platinum ring
241 conductivity electrode. Reported AOS values are the average of three separate
242 titrations for each sample, with standard deviations calculated based on the triplicate
243 measurements. The specific surface area of all samples was measured in duplicate
244 using the BET-N_2 method using a Gemini V2365 system (Micromeritics Instrument
245 Corp.). Samples were dried and degassed for 24 hr at room temperature. Reported
246 BET values are ±5 %.

In addition to the above analyses, we also collected extended X-ray absorption fine structure (EXAFS) spectra for our c-disordered birnessite precursor, Mg-exchanged phyllomanganate intermediate and subsequent reflux products at the Mn K-edge (6.539 keV). Spectra were collected on station B18 at Diamond Light Source (DLS) Ltd. During data collection, storage ring energy was 3.0 GeV and the beam current was approximately 200 mA. EXAFS data were collected from up to 6 transmission mode scans using a Ge 9-element detector. Test scans indicated no photo-reduction after 6 scans to k = 14 $Å^{-1}$. Nevertheless, in order to minimize beam damage we recorded 2 EXAFS spectra at a single x,y point before moving to a new point to record a further 2 spectra. For EXAFS measurements, dry powders were diluted with cellulose nitrate and pressed into pellets. Energy calibration was achieved by assigning the first inflection point of Au (L3) foil to 11.919 keV. EXAFS data reduction was performed using ATHENA (Ravel and Newville, 2005) and PySpline (Tenderholt et al., 2007). ATHENA was used to calibrate from monochromator position (millidegrees) to energy (eV) and to average multiple spectra from individual samples. PySpline was used to perform background subtraction where the pre-edge was fit to a linear function and the post-edge background to two 2nd-order polynomial segments.

2.4 Preparation of Reference Mn Oxides

A variety of synthetic Mn oxides were prepared and used as references during the above analyses. We synthesized triclinic Na-birnessite (Tc-Na-birnessite), crystalline hexagonal birnessite (Hx-birnessite), c-disordered hexagonal birnessite (as above), all with an interlayer spacing of ~7 Å, δMnO_2 and crystalline todorokite. Tc-Na-birnessite was prepared following the oxidation method of Liu et al., (2002), Hx-birnessite was prepared by acidification of the Tc-Na-birnessite suspension (Drits et al., 1997; Silvester et al., 1997; Lanson et al., 2000; Liu et al., 2002) and δMnO_2 was synthesized following the protocols of Villalobos et al. (2003). A todorokite with high crystallinity was prepared by hydrothermal treatment of a Mg-substituted Tc-Na-birnessite suspension, following the method of Feng et al. (1995). Synthesis procedures for the Tc-Na-birnessite, Hx-birnessite and todorokite are detailed in Peacock and Moon (2012). Mineral identity and purity of the references were confirmed by XRD analysis of randomly orientated powder samples.

3.0 RESULTS

3.1 X-ray Diffraction

C-disordered birnessite has basal reflections at ~7 Å [001] and ~3.5 Å [002] (for reference pattern see turbostratic birnessite, Drits et al., 1997), while for Mg-exchanged phyllomanganate these appear at ~10 Å [001] and ~5 Å [002] (for reference pattern see that of buserite JCPDS-32-1128). Exchange of Mg^{2+} ions into the interlayer of ~7 Å birnessite expands this region to ~10 Å. Both phases also have two *hk0* reflections (or *hk* bands) at ~2.4 Å [100] and ~1.4 Å [110]. These are due to diffraction within the phyllomanganate sheets. In common with 10 Å phyllomanganate, the tectomanganate todorokite has peaks at ~10 Å [001] and ~5 Å [002], and peaks at ~2.4-2.5 Å [21-1] and [210], and ~1.4 Å [020]. As such, it can be difficult to distinguish todorokite from 10 Å phyllomanganate using XRD (e.g., Burns et al., 1983, 1985; Giovanoli, 1985; Bodeï et al., 2007; Saratovsky et al., 2009; Feng et al., 2010). However, in contrast to 10 Å phyllomanganates, todorokite has characteristic peaks at 2.22 Å [21-2], 1.90 Å [31-2], 1.74 Å [21-4] and 1.54 Å [21-5] (JCPDS-38-475). In addition, the peak at ~2.4 Å [21-1] is prominent and the peak at ~2.5 Å is evident as a characteristic splitting of the ~2.4 Å phyllomanganate peak region when 10 Å phyllomanganate and todorokite are mixed. Compared to 10 Å phyllomanganate, todorokite also has a characteristic splitting of the ~5 Å peak to reveal a peak at ~4.3 Å, and displays a characteristic loss of symmetry and splitting of the ~1.4 Å peak.

XRD patterns for our c-disordered birnessite, Mg-phyllomanganate intermediate and all subsequent reflux products are presented in Figure 1. C-disordered birnessite shows 4 broad peaks at ~7.2 Å, ~3.6 Å, ~2.4 Å and ~1.4 Å originating from the [001], [002], [100] and the [110] reflections, respectively. After suspension of the c-disordered birnessite in 1 M $MgCl_2$ the basal spacing is expanded from ~7 Å to ~10 Å as indicated by the presence of both the ~9.6 Å [001] and ~4.8 Å [002] peaks in our Mg-phyllomanganate intermediate (Fig. 1). These peaks are more intense than those of the c-disordered birnessite precursor suggesting that the ion-exchange process enhances the crystallinity and long range ordering of the sheets. The $d100/d110$ peak intensity ratios for our c-disordered birnessite and Mg-phyllomanganate intermediate are 2.44/1.41 and 2.43/1.41 respectively, which equate to ~ $\sqrt{3}$ which is in good agreement with Villalobos et al. (2003) for c-disordered birnessite and indicates that the Mn layers have hexagonal symmetry with $a = b =$

2.83 Å (Drits et al., 1997). The ~1.4 Å peak is symmetrical in both our precursor and intermediate phases further indicating that these possess hexagonal symmetry (Drits et al., 2007). In both the precursor and intermediate phases the ~2.4 Å peak exhibits a degree of asymmetry on the high-angle side. This feature is typical of phyllomanganates that lack significant long-range ordering of the sheets (Villalobos et al., 2006). By contrast, triclinic birnessite (JCPDS-23-1046) shows a characteristic splitting of the peaks at ~2.4 Å and ~1.4 Å, lending the ~1.4 Å peak region in particular a distinctive asymmetry (e.g., Drits et al., 1997).

Over the course of the reflux four distinct changes are visible in the XRD patterns (Fig. 1). Firstly, the appearance of four broad peaks at ~2.2 Å, ~1.9 Å, ~1.7 Å and ~1.5 Å indicates that transformation of the 10 Å phyllomanganate to todorokite has begun by 3 hr reflux. As the reflux progresses, these peaks become sharper and more intense indicating the progressive formation of todorokite. Secondly, the peak at ~2.4 Å has split by 3 hr reflux to reveal two peaks in this region at ~2.45 and 2.41 Å, where the peak at ~2.45 Å becomes more prominent with time. Thirdly by 3 hr reflux, the peak at ~5 Å begins to broaden on the high-angle side, developing into a broad shoulder at ~4.3 Å, with two separate peaks distinguishable after 48 hr reflux. Finally, the ~1.4 Å peak shows a significant loss of symmetry as the reflux proceeds. These three later changes are those expected during the transformation of 10 Å phyllomanganate to todorokite (Feng et al., 2004) and are consistent with transformation having begun by 3 hr reflux.

3.2 Fourier Transform Infrared Spectroscopy

FTIR spectra for our c-disordered birnessite, Mg-phyllomanganate intermediate and a selection of the subsequent refluxed products are presented in Figure 2. For FTIR of Mn oxides, a broad peak at ~760 cm^{-1} is typically assigned to an asymmetrical Mn-O stretching vibration, corresponding to corner-sharing MnO_6 octahedra (Julien et al., 2004). This absorption band is absent in phyllomanganate (layer-type) Mn oxides and is therefore unique to those that possess a tectomanganate (tunnel-type) structure (Julien et al., 2004). FTIR spectroscopy can therefore conclusively distinguish between the layer-type intermediate phase and the tunnel-type todorokite product. Figure 2 shows that the characteristic peak is apparent in the refluxed product after 3 hr of reflux, which is consistent with the XRD data that also indicates the presence of todorokite by this time point (Fig. 1). The presence of the

348 760 cm^{-1} peak is consistent with a transition from edge- to corner-sharing MnO_6
349 octahedra, expected during the transformation of birnessite to todorokite (Julien et al.,
350 2004; Kang et al., 2007). The increasing intensity of this peak with time indicates that
351 more todorokite is present within the matrix as the transformation proceeds.
352
353 **3.3 Electron Microscopy**
354 SEM images of our c-disordered birnessite show that our precursor material
355 has a plate-like morphology typical of phyllomanganate Mn oxides (Fig. 3a).
356 Individual birnessite crystallites appear to be randomly oriented and aggregated into
357 larger particles measuring approximately 200-300 nm in diameter (not shown). After
358 6 hr reflux the overall morphology has evolved and small fibrous needles (<0.2 μm)
359 of todorokite can be seen intergrown within the platy birnessite matrix (Fig. 3b).
360 After 72 hr of reflux treatment, the mineralogy is dominated by elongated fibres (>
361 2.0 μm) of crystalline todorokite (Fig. 3c). In addition, these fibres appear to be
362 aggregated into a dense network of fibres displaying a plate-like morphology (Fig.
363 3d).
364 HR-TEM images are presented in Figure 4. The prominent feature of both the
365 c-disordered birnessite precursor (Fig. 4a, b) and the Mg-phyllomanganate
366 intermediate (Fig. 4c, d) is the repetition of the [001] lattice planes (space group
367 p63/mmc), from which we can infer that the individual phyllomanganate layers are
368 reasonably well stacked over at least 50 Å. The measured interlayer of the c-
369 disordered birnessite is equal to ~5.6 Å, while the Mg-phyllomanganate is equal to
370 ~8.6 Å (Fig. 4b, d), neither of which are consistent with the 7.2 Å and 9.6 Å *d*-
371 spacings determined via XRD (Fig. 1). However, it has been reported that
372 phyllomanganate layers are susceptible to collapse under the high vacuum conditions
373 required for TEM work. For example, Post and Veblen (1990) report layer collapse in
374 7 Å K^+ birnessite to ~6.0 Å. It is evident from Figure 4e that after approximately 1.5
375 hr reflux the phyllomanganate layers of the Mg-phyllomanganate have become
376 substantially rumpled and distorted in areas equivalent to several square nanometres.
377 In corroboration with our SEM observations (Fig. 3), TEM images taken after 6 hr
378 reflux (Fig. 4f) show a significant change in particle morphology. We observe
379 primary particles of todorokite that are ~ 8-10 nm wide and elongated longitudinally
380 along the [010] direction (space group p2/m; i.e., along the direction of tunnel growth)

381 some 200 nm in length (Fig. 4f). On close inspection at 6 hr reflux, these primary
382 particles appear to be aggregating together laterally across the [100] direction,
383 resulting in the formation of substantially wider todorokite laths that measure
384 approximately 20-30 nm in diameter, which is equivalent to the aggregation of 2-3
385 primary todorokite particles (Fig. 4f). The extent of lateral particle aggregation over
386 the duration of the experiment is highlighted in Figure 4, where we observe
387 significant lateral aggregation from 6 hr reflux (image 4f; laths on average ~ 20-30
388 nm wide), to 48 hr reflux (image 4g; laths on average ~ 50-100 nm wide) to 72 hr
389 reflux (image 4h; laths on average ~100-150 nm wide). In addition to lateral
390 aggregation, the particles also continue to elongate along the [010] direction as the
391 reflux proceeds (from 6 to 24 to 72 hr, images Fig. 4f, i and h, respectively). It is
392 difficult to determine from these images whether particle-particle aggregation along
393 the [010] makes any contribution to todorokite growth as, unlike across the [100]
394 direction, the observation of particle-particle boundaries is less clear. However, after
395 24 hr reflux, crystalline laths up to 600 nm in length ([010] direction) are observed
396 extending from central regions of overlapping todorokite laths (Fig. 4i). The central
397 regions of overlapping laths are aligned with each other at 120°. This dense network
398 of fibres gives rise to the formation of large aggregates of todorokite that exhibit a
399 plate-like morphology. The size of these plate-like aggregates appears to increase
400 with increased reflux time and, after 72 hr, plates of todorokite measuring
401 approximately 500 x 550 nm are observed (Fig. 4j). This plate-like growth
402 morphology is typical of todorokite found in both marine and terrestrial settings
403 (Turner et al., 1982; Siegel and Turner 1983; Bodeï et al., 2007; Xu et al., 2010).
404 HR-TEM images (Fig. 4k, j) also reveal that the todorokite product contains a
405 number of structural defects. Specifically, the todorokite tunnels highlighted in
406 Figure 4k display widths across the [100] direction of ~ 6 Å, 9 Å and 16 Å,
407 approximately corresponding to tunnels that are (3x2), (3x3) and (3x4) MnO_6
408 octahedra wide. Tunnel-width inconsistencies are commonly observed in todorokite
409 (Turner et al., 1982; Feng et al., 2004; Bodeï et al., 2007; Xu et al., 2010). In addition
410 to heterogeneous tunnel dimensions, the images also reveal the presence of a
411 substantial number of linear dislocations along the direction of tunnel growth (Fig.
412 4j).
413
414

415 **3.4 Physiochemical Characterization**

416 The surface area and pH measurements for our c-disordered birnessite, Mg-
417 phyllomanganate intermediate and all subsequent reflux solids and solutions,
418 respectively, are presented in Table 1 and Figure 5. The measured N_2 BET surface
419 areas of the c-disordered birnessite and Mg-phyllomanganate intermediate are 103.7
420 m^2/g and 104.9 m^2/g, respectively. After 3 hr reflux the surface area has decreased to
421 78.82 m^2/g and shows little variation during the first 12 hr, with all measured values
422 falling within the 5 % error range of the technique. The measured surface area then
423 peaks at 95 m^2/g at 24 hr, after which there is a subsequent drop to 69.95 m^2/g at 48
424 hr, ending with 65.82 m^2/g at 72 hr. The pH values of the reflux solutions at 3 hr until
425 24 hr show little variation, averaging at 4.85 pH units. At 48 hr there is an increase in
426 pH to 5.10, which further increases to 5.51 pH units at 72 hr reflux. An increase in
427 solution pH towards the end of the reflux procedure is consistent with Feng et al.
428 (2010).

429 The Mn AOS in c-disordered birnessite is 3.78±0.04. This value is in good
430 agreement with Villalobos et al. (2003) for c-disordered birnessite and indicates that
431 the precursor contains a significant proportion of Mn(III). After exchange in 1 M
432 $MgCl_2$ the AOS is 3.75±0.04, while after 72 hr reflux the final todorokite product has
433 an AOS of 3.79±0.004. Our titration results indicate that within error there is no
434 significant change in the net Mn AOS as the transformation proceeds.

435

436 **3.5 X-ray Absorption Spectroscopy**

437 Mn K-edge EXAFS of the reference Mn oxides, our c-disordered birnessite,
438 Mg-phyllomanganate intermediate and early stage reflux products are shown in
439 Figure 6. Mn EXAFS spectroscopy is sensitive to Mn-O and Mn-Mn interatomic
440 distances, and MnO_6 polyhedral linkages (e.g., Manceau and Combes, 1988).
441 Information on sample mineralogy and crystallinity can therefore be obtained by
442 comparing sample spectra to a suite of standard Mn oxide reference spectra (e.g.,
443 Manceau et al., 2002). In agreement with previous studies, our Mn oxide reference
444 spectra show clear differences in *k*-space in the (6.5 – 9.5 $Å^{-1}$) indicator region (e.g.,
445 Webb et al., 2005a). This region is sensitive to the amount and ordering of Mn(IV)
446 and Mn(III) in the sheets of phyllomanganates (δMnO_2, c-disordered birnessite, Hx-
447 birnessite and Tc-Na-birnessite) and to the tunnel dimension in tectomanganates

448 (todorokite) (e.g., Manceau and Combes, 1988; McKeown and Post, 2001). In
449 particular, the *k*-space peaks at ~6.7, 8 and 9.2 $Å^{-1}$ appear sharper and more intense
450 for layered vs. tunnel structures (e.g., Webb et al., 2005a). This is evident when
451 comparing our phyllomanganate (δMnO_2 and Hx-birnessite) to our tectomanganate
452 (high crystalline todorokite) reference spectra. For layered structures, these indicator
453 features also appear sharper and more intense with an increase in coherent stacking of
454 the layers along the c-axis, i.e., from δMnO_2, to c-disordered birnessite, to Hx-
455 birnessite (e.g., Webb et al., 2005a). As expected, our spectra show that our c-
456 disordered birnessite precursor and Mg-phyllomanganate intermediate, have c-axis
457 ordering that is intermediate between turbostratic δMnO_2 and highly crystalline Hx-
458 birnessite (Fig. 6). In addition, in agreement with our XRD, our Mg-
459 phyllomanganate intermediate displays slightly sharper and more intense indicator
460 peaks than our c-disordered birnessite precursor, confirming that the ion-exchange
461 process enhances the c-axis ordering of the Mn octahedral layers. Mn K-edge
462 EXAFS can also be used to conclusively distinguish between phyllomanganates with
463 triclinic and hexagonal symmetry, where triclinic phases exhibit a splitting of the
464 indicator peak at ~8 $Å^{-1}$ while hexagonal phases do not (Webb et al., 2005). In this
465 respect our spectra confirm that our c-disordered birnessite precursor has hexagonal
466 symmetry, in agreement with our XRD (Fig. 1) and as expected for c-disordered
467 birnessite synthesized following the method of Villalobos et al. (2003). Our spectra
468 also show that our Mg-phyllomanganate intermediate and early-stage reflux products,
469 shown until 3 hr reflux (by which time we have visually observed rumpling of the
470 phyllomanganate layers at 1.5 hr (Fig. 4e)), similarly possess hexagonal symmetry.
471
472
473 **4.0 DISCUSSION**
474 **4.1 Mechanism of Todorokite Formation in the Marine Environment**
475 It is widely agreed that the formation of todorokite in the marine environment
476 is a complex multistage process (Burns and Burns, 1978a,b; Siegel and Turner, 1983;
477 Golden et al., 1986; Shen et al., 1993; Feng et al., 2004; Bodeï et al., 2007; Feng et
478 al., 2010). The exact formation mechanism of todorokite in marine diagenetic and
479 hydrothermal settings has remained unclear due to this complexity, and because it is
480 often found intermixed with other poorly crystalline oxyhydroxide minerals (Usui et

481 al., 1997; Banerjee et al., 1999; Bodeï et al., 2007). Todorokite was initially
482 synthesized by Golden et al. (1986), however subsequent confirmation of this
483 synthesis has often proved challenging (Siegel and Turner, 1983; Golden et al., 1986;
484 Shen et al., 1993; Ching et al., 1999; Feng et al., 2004; Cui et al., 2006; Cui et al.,
485 2008; Cui et al., 2009; Feng et al., 2010).

486 The current experimental study presents the first detailed description of the
487 crystallization pathway and mechanism of todorokite formation from birnessite. We
488 show that this reaction pathway involves a four-stage process beginning with
489 todorokite nucleation, then crystal growth to form todorokite primary particles,
490 followed by their self-assembly and oriented growth, culminating in a traditional
491 crystal ripening processes. Each of these stages in the crystallization process is
492 described in detail below.

493

494 *4.1.1 Todorokite nucleation*

495 Previous studies have recognized that the ordering of the birnessite layers over
496 at least several tens of angstroms is fundamental for the eventual formation and
497 pillaring of the todorokite tunnel walls (e.g., Bodeï et al., 2007). HR-TEM of our
498 birnessite precursor and 10 Å phyllomanganate intermediate indicates that the
499 individual phyllomanganate layers are reasonably well stacked over at least 50 Å (Fig.
500 4b, d). It has also been suggested that the presence of structural Mn(III) within the
501 birnessite layers is an important prerequisite for todorokite formation (Bodeï et al.,
502 2007; Cui et al., 2008). Specifically, distortion of the Mn(III) octahedra due to the
503 Jahn-Teller effect results in the elongation and thus weakening of the Mn^{3+}-O bonds
504 along the z-axis. It is at this structural weak point, between the Mn^{3+}-O-Mn^{4+} bonds
505 that run parallel to the [010], that the phyllomanganate layers are thought to be most
506 susceptible to rumpling (Bodeï et al., 2007; Cui et al., 2008). It is believed that this
507 kinking of the layers leads to the formation of the todorokite tunnel walls within the
508 volume of the phyllomanganate interlayer (Bodeï et al., 2007; Cui et al., 2008).
509 Potentiometric titration of our birnessite precursor and 10 Å phyllomanganate
510 intermediate confirm that these two phases contain a significant proportion of Mn(III),
511 with AOS of 3.78 and 3.75, respectively. We directly observe the proposed rumpling
512 of the phyllomanganate layers at 1.5 hr reflux. Specifically, HR-TEM images
513 indicate that the layers of the 10 Å intermediate have become distorted in localized
514 areas some tens of square nanometers in size (Fig. 4e). This suggests that the

515 rearrangement of the phyllomanganate sheets, and thus the nucleation of todorokite,
516 proceeds within local domains relatively rapidly after the start of reflux treatment.
517 Furthermore, Cui et al. (2006) investigate the transformation of birnessite to
518 todorokite over a wide temperature range from 40 to 140 ^{o}C, and show that the
519 transformation is significantly enhanced at and above 100 ^{o}C. In parallel, Bodeï et al.
520 (2007) suggest that elevated temperatures increase the kinetics of the 10 Å
521 intermediate transformation. With our new data we suggest specifically that the
522 kinking of the 10 Å phyllomanganate layers, and thus the key step in the nucleation of
523 todorokite, is thermally induced. The temperature dependence of todorokite
524 nucleation then at least partly explains the prevalence of todorokite over
525 phyllomanganates in hydrothermal marine ferromanganese precipitates (as
526 documented by, for example, Burns and Burns (1977)).

527 Based on the literature to date and our new data presented here, it is clear that
528 there are two major prerequisites for the formation of crystalline todorokite directly
529 from 10 Å phyllomanganate. Firstly, the 10 Å phase must contain enough structural
530 Mn(III) to allow the kinking of the phyllomanganate layers. Secondly, the 10 Å phase
531 must also display at least semi-coherent c-axis ordering, so that as the
532 phyllomanganate layers kink, there are sufficient adjacent layers for the cross-linking
533 todorokite tunnel walls to form. The absence of one or both of these prerequisites
534 results in the synthesis of a variety of layer-type and tunnel-type Mn oxide products.
535 For example, Feng et al. (2010) use a biogenic phyllomanganate precursor with AOS
536 3.8±0.3 but incoherent (turbostratic) c-axis ordering, and are able to produce only a
537 very poorly crystalline nanoscale todorokite-like product; these authors also report a
538 failed attempt to synthesize todorokite from an acid birnessite with semi-coherent c-
539 axis ordering but an AOS of 3.96±0.02. Similarly, Bodeï et al. (2007), using a
540 turbostratic 10 Å phyllomanganate, produce a mixture of primary 7 Å birnessite and
541 jianshuite/Mg-chalcophanite and secondary poorly crystalline todorokite. It has also
542 been suggested that triclinic symmetry in the 10 Å phyllomanganate intermediate
543 might be another prerequisite for todorokite formation (Feng et al., 2010), i.e., that
544 during the formation of todorokite from hexagonal 7 Å birnessite, there is a
545 transformation from hexagonal symmetry in the precursor to triclinic symmetry in the
546 intermediate phase. We have shown from our XRD and Mn K-edge EXAFS (Fig. 6)
547 however, that both our precursor and intermediate phases possess hexagonal
548 symmetry, and we see no evidence for the appearance of a triclinic phyllomanganate

549 during the early stages of todorokite nucleation. It therefore appears that todorokite
550 can form via a hexagonal pathway and triclinic symmetry is not a prerequisite for
551 todorokite formation.
552
553 *4.1.2 Formation of todorokite primary particles*
554 After the formation of todorokite nucleation sites by 1.5 hr reflux, FTIR data
555 (Fig. 2) confirms that by 3 hr reflux there is some degree of structural transition from
556 edge-sharing to corner-sharing MnO_6 octahedra as indicated by the appearance of the
557 broad shoulder at ~760 cm^{-1} in the FTIR spectrum (Julien et al., 2004; Kang et al.,
558 2007). In turn this is consistent with our XRD data (Fig. 1) at 3 hr reflux, which
559 shows the presence of characteristic todorokite peaks between 2.4 Å and 1.5 Å.
560 Notably, we observe an increase in asymmetry of the initially symmetrical 10 Å
561 intermediate [110] reflection as it evolves into the todorokite [020] reflection, with
562 this trend towards asymmetry beginning by 3 hr reflux. The growth and narrowing of
563 the todorokite [020] reflection reflects todorokite growth along the [010] direction,
564 i.e., along the direction of tunnel growth.
565 We capture the first visual evidence of todorokite crystallization at 6 hr reflux
566 with the clear presence of small and poorly crystalline primary particles of todorokite
567 in the TEM images (Fig. 4f). Interestingly, these primary particles are elongated
568 along the [010] direction, measuring up to 200 nm in length (Fig. 4f). By comparison,
569 the width of these particles along the [100] direction is significantly smaller,
570 measuring between 8 and 10 nm. The widths of the todorokite particles are
571 comparable to the crystallite size (calculated from Scherer analysis) of the 10 Å
572 phyllomanganate intermediate particles i.e. ~8 nm along the [100] direction. We
573 suggest that following the nucleation of todorokite within the phyllomanganate layers,
574 the todorokite particles grow preferentially along the [010] direction with the width of
575 the particles controlled by the crystallite size of the phyllomanganate intermediate i.e.
576 ~8 nm. Due to the difference in both size and morphology between the 10
577 Å phyllomanganate and todorokite, we suggest that the todorokite primary particles
578 grow along the [010] via dissolution of the 10 Å phyllomanganate followed by
579 precipitation of crystalline todorokite. This is consistent with the drop in surface area
580 measured between the 10 Å phyllomanganate intermediate and the reflux product at 3
581 hr.
582

583

584 *4.1.3 Self-assembly and oriented growth*

585 It is evident on close inspection (Fig. 4f) that at 6 hr reflux some of the
586 initially formed primary particles of todorokite are orientated and aggregated together
587 laterally across the [100] direction resulting in the formation of substantially wider
588 todorokite laths (20-30 nm wide). It is possible to make out several particle-particle
589 boundaries between laterally aggregating primary particles (Fig. 4f). However,
590 similarly early on in the transformation it is difficult to identify any particle-particle
591 boundaries along the length of tunnel growth. This suggests that primary particle
592 aggregation is occurring exclusively in the lateral direction. Our data therefore
593 indicate that following the formation of acicular todorokite, the primary crystallites
594 aggregate via attachment of the [100] faces i.e., via oriented attachment. This is again
595 consistent with the drop in surface area from the 10 Å phyllomanganate intermediate
596 to the 3 hr reflux product. Analysis of our HR-TEM data shows that there is little
597 variation in the widths of individual todorokite primary particles from the early stages
598 of particle nucleation (widths on average ~ 8 nm) to the end of the reflux treatment
599 (widths on average ~ 5-15 nm). This indicates that lateral oriented attachment of
600 todorokite particles is a key particle growth mechanism throughout the duration of the
601 reflux treatment. The progressive attachment of todorokite primary particles is
602 consistent with the overall drop in surface area from the 3 hr to 72 hr reflux products
603 (Fig. 5). The maximum surface area value measured at 24 hr reflux may therefore be
604 an anomaly. The self-assembly and lateral aggregation of primary particles in an Mn
605 oxide system has also been observed by Portehault et al. (2007) during the formation
606 of cryptomelane. They find that cryptomelane-type MnO_2 nanowires synthesized
607 under mild hydrothermal conditions form via the lateral "side to side" aggregation of
608 primary nanorods.

609 Oriented attachment (OA) refers to the self-assembly and oriented growth of
610 primary particles to form larger secondary particles. First described by Penn and
611 Banfield (1998a), OA is a spontaneous crystal growth mechanism, whereby primary
612 crystallites align and eventually aggregate together at specific surfaces that share
613 similar crystallographic dimensions. The resulting secondary particles are larger and
614 thus ultimately more thermodynamically stable due to the overall reduction in surface
615 free energy (Penn and Banfield, 1998a, b). In recent years the importance of this non-
616 classical growth mechanism has become increasingly apparent and a growing number

617 of studies have shown that under varying experimental conditions a diverse range of
618 geochemically important mineral phases such as Fe oxides, TiO_2, ZnS and $CaSO_4$
619 form via OA-based growth mechanisms (Penn and Banfield, 1998a; Penn and
620 Banfield, 1999; Banfield et al., 2000; Gilbert et al., 2003; Huang et al., 2003;
621 Waychunas et al., 2005; Burrows et al., 2012; Van Driessche et al., 2012). In
622 addition, the growth of materials by OA has also been shown to provide a route for
623 the formation of a variety of structural defects (Penn and Banfield et al., 1998a, b;
624 Penn et al., 2001). For example, it is understood that prior to attachment, particles
625 may often misalign, ultimately leading to the offset of lattice planes between
626 adjoining particles. This misalignment leads to the incorporation of both linear- and
627 edge-type dislocations at particle-particle boundaries (Penn and Banfield, 1998a;
628 Banfield et al., 2000; Penn et al., 2001) such as those observed in the microstructure
629 of our neo-formed todorokite samples (Fig. 4j).

630 Notably, in addition to formation of laths, in our todorokite system we also
631 observe that individual laths are oriented specifically in three distinct directions at
632 60°/120° to each other (Fig. 4j) to form large aggregates of todorokite with a plate-
633 like morphology. This trilling pattern is a characteristic growth morphology of
634 todorokite that has been widely described in both natural and synthetic samples
635 (Seigel and Turner, 1983; Golden et al., 1987; Feng et al., 2004; Bodeï et al., 2007;
636 Xu et al., 2010). We suggest that this morphology arises due to the assembly and
637 subsequent attachment of adjacent layers of elongated todorokite laths, on the [001]
638 faces. Because of the pseudo-hexagonal structure within the Mn-O layers of the
639 todorokite, adjacent layers can attach with a 60°/120° angle between the layers and
640 still provide structural continuity, with each stacked layer having elongated
641 crystallites aligned in one direction.

642 In summary, we suggest that the formation of todorokite from birnessite
643 proceeds via the initial formation of local nano-domains of todorokite within the 10 Å
644 phyllomanganate interlayer, leading to the formation of primary todorokite particles
645 that grow from solution exclusively along the [010] direction. These primary
646 particles then self-assemble laterally across the [100] direction via OA to form
647 significantly larger and more crystalline secondary todorokite laths. Todorokite laths
648 may undergo further assembly, to form stacked layers, in which laths of todorokite
649 may attach at angles of 60º, 120º or 240º in order to retain structural continuity. This
650 process is presented visually in Figure 7. To our knowledge this is the first study to

observe primary todorokite particles and capture their self-assembly and oriented growth during todorokite formation.

In order to robustly relate our formation and growth mechanism to the formation of todorokite in the marine environment, it is necessary to consider the role of artificial reflux treatment on the overall transformation process. It has been shown that the growth of materials via hydrothermal routes typically favours OA-type growth (Penn and Banfield 1999; Gilbert et al., 2003; Lee et al., 2005). Importantly however, the morphological growth features observed in our synthetic samples throughout the reflux process are highly comparable to those seen in natural marine todorokite. As such, while the refluxing process necessarily accelerates the transformation rate, the overall formation and growth mechanism does not appear to have been fundamentally altered.

4.1.4 Ripening

In many instances experimental observations have shown that growth by OA usually dominates during the early stages of crystallization, and subsequently gives way to traditional ripening-based growth during the final stages of crystallization (Waychunas et al., 2005; Zhang et al., 2009). We therefore suggest that our neo-formed todorokite undergoes further growth from solution as a result of Ostwald-ripening during the later stages of the reflux, once any remaining birnessite has been transformed. However, owing to overlap of key peaks in the diffraction patterns of our 10 Å intermediate phase and the final todorokite product it is difficult to elucidate when the transformation is complete, and thus when all birnessite is consumed and ripening occurs. The significant decrease in surface area at 48 hr and 72 hr reflux is consistent with crystal ripening.

4.2 Implications for Trace Metal Cycling in Marine Sediments

It is well understood that the sequestration of dissolved trace metals to Mn oxide phases, and in particular to the phyllomanganate birnessite, exerts a strong control on the concentration of metals in seawater (e.g., Goldberg, 1954; Cronan, 1976; Burns and Burns, 1979; Post, 1999; Peacock and Sherman, 2007a; Sherman and Peacock, 2010; Spiro et al., 2010). In particular, recent work shows that sorption equilibrium between marine birnessite and the micronutrients Ni and Cu helps explain measured concentrations of these metals in the modern global oceans (Peacock and

685 Sherman, 2007a; Sherman and Peacock, 2010). Mechanistically, Ni and Cu are
686 sequestered from seawater and strongly bound to birnessite (e.g., Manceau et al.,
687 2007a; Peacock and Sherman, 2007a; Peacock, 2009; Sherman and Peacock 2010),
688 where at the pH of seawater and marine sediment porewaters, these metals then
689 become variably progressively incorporated into the birnessite structure with time
690 (Peacock, 2009; Peña et al., 2010; Sherman and Peacock, 2010). In natural marine
691 birnessite, Ni is found entirely structurally incorporated (Peacock and Sherman,
692 2007b) while Cu only partially incorporates, likely because Cu(II) is Jahn-Teller
693 distorted while Ni(II) is not (Sherman and Peacock, 2010). Jahn-Teller distortion
694 sterically hinders Cu(II) incorporation into Mn(IV)-rich birnessite.

695 In the context of the current study, it is traditionally thought that Ni and Cu
696 incorporated into birnessite might aid its transformation to todorokite (Burns and
697 Burns, 1978; Burns and Burns, 1979; Usui, 1979; Takematsu et al, 1984).
698 Subsequent work suggests specifically that the incorporation of heterovalent cations,
699 including Mn(III), Ni(II) and Cu(II), is necessary to kink the 10 Å phyllomanganate
700 layers (Bodeï et al., 2007). For Mn(III) at least, we support this assertion and show
701 that the kinking of the 10 Å phyllomanganate layers leads to the nucleation of
702 todorokite primary particles. However, despite the role of Mn(III) in the
703 crystallization of todorokite, it has been noted that natural todorokite typically
704 contains significantly less Ni and Cu than the 10 Å phyllomanganate from which it
705 crystallized (Siegel and Turner, 1983; Bodeï et al., 2007). For example, Siegel and
706 Turner (1983) report 10 Å phyllomanganate with 3.8% NiO and 2.8% CuO while the
707 neo-formed todorokite contains only 0.2% NiO and 1.5% CuO. While these studies
708 do not explain the overall lower amounts of metal impurities in neo-formed
709 todorokites, Siegel and Turner (1983) do suggest that higher Cu concentrations in
710 todorokite reflect the Jahn-Teller distortion of Cu(II), and thus incorporated Cu(II)
711 (and specifically the strained Cu^{2+}-O-$Mn^{3/4+}$ bond) is more favourable for kinking of
712 the phyllomanganate layers and thus formation of Cu-bearing todorokite.

713 Having determined a four-stage nucleation and growth mechanism for the
714 formation of todorokite, we can shed new light on the role of trace metal impurities,
715 and their ultimate fate, during transformation. We suggest that, in fact, only
716 incorporated heterovalent cations with Jahn-Teller distortion will facilitate the initial
717 kinking of the 10 Å phyllomanganate layers and thus promote the nucleation of
718 todorokite and the subsequent formation of todorokite primary particles. It follows

that for Ni-rich 10 Å phyllomanganates (where Ni(II) is not Jahn-Teller distorted), and in particular those with low structural Mn(III) and/or Cu(II) content, Ni(II) might retard the transformation of birnessite to todorokite, and/or be lost to solution in order that transformation can proceed, both of which potentially explain the prevalence of Ni-poor todorokites in the natural environment. Studies investigating the role of trace metal impurities during growth by OA are extremely limited, especially for cases where growth by OA is accompanied by phase transformation or vice versa. Kim et al. (2008) indicate that metal(loids) adsorbed to goethite nanoparticle surfaces substantially disrupt growth via OA, by essentially blocking attachment and aggregation interfaces. These authors conclude that if nanoparticle growth by OA is to proceed, impurities at aggregation interfaces must either be incorporated into the mineral structure away from attachment surfaces or desorbed into solution. Because the Mn octahedral layers in both birnessite and 10 Å phyllomanganate are only a single octahedron thick, impurities incorporated into the mineral structure are effectively still present at aggregation interfaces. If non Jahn-Teller distorted impurities are lost to solution then the diagenesis of birnessite potentially provides a source of these metals to marine sedimentary pore-waters and subsequently a benthic flux of micronutrients to seawater. In order to investigate the role of Jahn-Teller vs. non Jahn-Teller cations in the nucleation and growth of todorokite, similar experiments to those in this work are required, but using, for example, Cu- and Ni-doped birnessite precursors. Comparison of these experiments to the work reported here would elucidate the effect of metal impurities on the rate and mechanism of transformation, and determine the fate of the impurities as the transformation proceeds.

5. SUMMARY AND CONCLUSIONS

The current study provides the first detailed mechanism for the formation and growth of todorokite from birnessite in the marine environment. Specifically, we present evidence for a four-stage process that can be summarized as:

1. Nucleation of todorokite: Todorokite tunnel walls form within the phyllomanganate interlayers via kinking of the layers, these nano-domains then provide a nucleation site for todorokite primary particle formation.

2. Primary particle formation: Primary todorokite particles grow from solution via dissolution-recrystallization, specifically along the direction of tunnel growth ([010] direction).
3. Oriented attachment of primary particles: Simultaneous with their growth from solution, the primary particles align and attach perpendicular to the direction of tunnel growth ([100] direction) via oriented attachment, to form todorokite laths.
4. Ripening: Once the birnessite is consumed, further growth from solution occurs via Ostwald-ripening.

We propose there are two prerequisites for the formation of todorokite from 10 Å phyllomanganate. Firstly, the 10 Å phyllomanganate must contain a significant proportion of structural Mn(III) which, due to its Jahn-Teller distortion, facilitates kinking of the layers. Secondly, the 10 Å phyllomanganate must also display semi-coherent c-axis ordering, so that as the layers kink, there are sufficient adjacent layers for the formation of the todorokite tunnel walls. Both of these factors are necessary for the nucleation of todorokite and subsequent formation of todorokite primary particles.

Based on these prerequisites it follows that, contrary to traditional thinking, only structural cation impurities with Jahn-Teller distortion will aid the formation and growth of todorokite. As such, we predict that structural cation impurities without Jahn-Teller distortion (e.g., Ni) might retard the transformation of birnessite to todorokite and/or be lost to solution during this diagenetic process. We suggest that the diagenesis of birnessite might provide a source of trace metals to marine sedimentary pore-waters and thus potentially a benthic flux of these micronutrients to seawater.

Acknowledgments

We thank Michael Ward and Eric Condliffe (Leeds Electron Microscopy and Spectroscopy Centre) for assistance with TEM and SEM imaging, respectively. We thank Adrian Cunliffe (Faculty of Engineering, Leeds University) for assistance with FTIR Spectroscopy. We thank Diamond Light Source for access to beamline B18 (grant SP7326) which contributed to the results presented here. We thank Stephen Parry, Giannantonio Cibin and Andrew Dent (Diamond Light Source Ltd.) for support at station B18. A. L. Atkins was supported via a NERC studentship. We also thank

three anonymous reviewers and the Associate Editor for their helpful comments to improve our manuscript.

REFERENCES

Arrhenius G. (1963) Pelagic sediments. In *Sea*, vol. 3 (ed. M. N. Hill). Interscience, New York, pp. 655–727.

Banerjee D. and Nesbitt H. W. (1999) Oxidation of aqueous Cr (III) at birnessite surfaces: constraints on reaction mechanism. *Geochim. Cosmochim. Acta* **63**, 1671–1687.

Banfield J. F., Welch S. A., Zhang H., Ebert T. T. and Penn R. L. (2000) Aggregation-based crystal growth and microstructure development in natural iron oxyhydroxide biomineralization products. *Science* **289**, 751–754.

Bargar J. R., Tebo B. M., Villinski J. E. (2000) In situ characterization of Mn (II) oxidation by spores of the marine Bacillus sp. strain SG-1. *Geochim. Cosmochim. Acta* **64**, 2775–2778.

Bargar J. R., Tebo B. M., Bergmann U., Webb S. M., Glatzel P., Chiu V. Q. and Villalobos M. (2005) Biotic and abiotic products of Mn (II) oxidation by spores of the marine Bacillus sp. strain SG-1. *Am. Mineral.* **90**, 143–154.

Bodeï S., Manceau A., Geoffroy N., Baronnet A., Buatier, M. (2007) Formation of todorokite from vernadite in Ni-rich hemipelagic sediments. *Geochim. Cosmochim. Acta* **71**, 5698–5716.

Brouwers G. J., Vijgenboom E., Corstjens P. L. A. M., De Vrind J. P. M., De Vrind-De Jong E. W. (2000) Bacterial Mn^{2+} Oxidizing Systems and Multicopper Oxidases: An Overview of Mechanisms and Functions. *Geomicrobiol. J.* **17**, 1-24.

Burns R. G. and Burns V. M. (1977) Mineralogy of ferromanganese nodules. In *Marine Manganese Deposits* (ed. G. P. Glasby). Elsevier, Amsterdam.

Burns V. M. and Burns R. G. (1978a) Authigenic todorokite and phillipsite inside deep-sea manganese nodules. *Am. Mineral.* **63**, 827-831.

Burns V. M. and Burns R. G (1978b) Post-depositional metal enrichment processes inside manganese nodules from the north equatorial pacific. *Earth Planet. Sci. Lett*. **39**, 341-348.

Burns R. G. and Burns V. M. (1979): Manganese oxides. In *Marine Minerals* (ed. R. Burns). *Rev. Mineral*. **6**, l-46.

Burns R. G., Burns V. M. and Stockman H. (1983) A review of the todorokite buserite problem: implications to the mineralogy of marine manganese nodules. *Am. Mineral.* **68**, 972–980.

Burns R. G., Burns V. M. and Stockman H. (1985) The todorokite–buserite problem: further consideration. *Am. Mineral.* **70**, 205–208.

Burrows N. D., Hale C. R. H., Penn R. L. (2012) Effect of ionic strength on the kinetics of crystal growth by orientated aggregation. *Cryst. Growth. Des.* **12**, 4787-797.

Calvert S. E. and Price N. B. (1970) Composition of manganese nodules and manganese carbonates from Loch Fyne, Scotland. *Contrib. Mineral. Petrol.* **29**, 215-233.

Ching S., Krukowska K. S. and Suib S. L. (1999) A new synthetic route to todorokite-type manganese oxides. *Inorg. Chim. Acta* **294**, 123–132.

Cronan D. S. (1976) Basal metalliferous sediments from the eastern Pacific. *Bull. Geol. Soc. Amer.* **87**, 928-934.

Cui H. J., Feng X. H., He J. Z., Tan W. F. and Liu F. (2006) Effects of reaction conditions on the formation of todorokite at atmospheric pressure. *Clays Clay Miner*. **54**, 605–615.

Cui H. J., Liu X. W., Tan W. F., Feng X. H., Liu F. and Ruan H. D. (2008) Influence of Mn(III) availability on the phase transformation from layered buserite to tunnel-structured todorokite. *Clays Clay Miner*. **56**, 397–403.

Cui H. J., Qiu G. H., Feng X. H., Tan W. F. and Liu F. (2009a) Birnessites with different average manganese oxidation states were synthesized, characterized, and transformed to todorokite at atmospheric pressure. *Clays Clay Miner*. **57**, 715–724.

Drits V. A., Silvester E., Gorshkov A. L. and Manceau A. (1997) Structure of synthetic monoclinic Na-rich birnessite and hexagonal birnessite: I. Results from X-Ray diffraction and selected area electron diffraction. *Am. Mineral*. **82**, 946-961.

Drits V. A., Lanson B. and Gaillot A.-C. (2007) Birnessite polytype systematics and identification by powder X-ray diffraction. *Am. Mineral*. **92**, 771–788.

Feng Q., Kanoh H., Miyai Y. and Ooi K. (1995) Metal ion extraction/insertion reactions with todorokite-type manganese oxide in the aqueous phase. *Chem. Mater*. **7**, 1722–1727.

Feng Q., Yanagisawa K. and Yamasaki N. (1998) Hydrothermal soft chemical process for synthesis of manganese oxides with tunnel structures. *J. Porous Mater.* **5**, 153–161

Feng X. H., Tan W. F., Liu F., Wang J. B. and Ruan H. D. (2004) Synthesis of todorokite at atmospheric pressure. *Chem. Mater*. **16**, 4330–4336.

Feng X. H., Zhu M., Ginder-Vogel M., Ni C., Parikh S. J., Sparks D. L. (2010) Formation of nano-crystalline todorokite from biogenic Mn oxides. *Geochim. Cosmochim. Acta* **74**, 3232–3245.

Francis C. A., Co E. M., Tebo B. M. (2001) Enzymatic manganese (II) oxidation by a marine alpha-proteobacterium. *Appl. Environ. Microbiol.* **67,** 4024-4029.

Friedl G., Wehrli B., and Manceau A. (1997) Solid phases in the cycling of manganese in eutrophic lakes: New insights from EXAFS spectroscopy. *Geochim. Cosmochim. Acta* **61**, 275–290.

Gaillot A-C. (2002) Caracterisation structurale de la birnessite: Influence du protocole de synthese. Ph.D thesis, Universite Joseph Fourier- Grenoble.

Gilbert B., Zhang H., Huang F., Finnegan M. P., Waychunas G. A., Banfield J. F. (2003) Special phase transformation and crystal growth pathways observed in nanoparticles. *Geochem. Trans.* **4,** 20-27.

Giovanoli R., Biirki P., Giuffredi M. and StummW. (1975) Layer Structured Manganese Oxide Hydroxides. IV. The Buserite Group; Structure Stabilization by Transition Elements. *Chimia*. **29**. 517-52.

Giovanoli R. (1985) A review of the todorokite-buserite problem: implications to the mineralogy of marine manganese nodules: discussion. *Am. Mineral.* **70**, 202-204.

Goldberg E. D. (1954) Marine geochemistry. I. Chemical scavengers of the sea. *J. Geol*. **62**, 249–265.

Golden D. C., Chen C. C. and Dixon J. B. (1986) Synthesis of todorokite. *Science* **231**, 717–719.

Golden D. C., Chen C. C. and Dixon J. B. (1987) Transformation of birnessite to buserite, todorokite and manganite under mild hydrothermal treatment. *Clays Clay Miner.* **35**, 271-280.

Grangeon S., Lanson B., Lanson M. and Manceau A. (2008) Crystal structure of Ni-sorbed synthetic vernadite: a powder X-ray diffraction study. *Mineral Mag*. **72**, 1279–1291.

Huang F., Zhang H and Banfield J. F (2003) The role of orientated attachment crystal growth in hydrothermal coarsening of Nano crystalline ZnS. *J. Phys. Chem B*. **107**, 10470-10475.

Jauhari P. (1987) Classification and inter-element relationships of ferromanganese nodules from the Central Indian Ocean Basin. *Marine Minerals* **6**, 419-429.

Julien C. M., Massot M., Poinsignon S. (2004) Lattice vibrations of manganese oxides part I. Periodic structures. *Spectrochim. Acta. A.* **60**, 689-700.

Kang L., Zhang M., Liu Z. H., Ooi K. (2007) IR spectra of manganese oxides with either layered or tunnel structure. *Spectrochim Acta*. **67**, 864-869.

Kim C. S., Lentini C. J. and Waychunas G. A. (2008) Associations between iron oxyhydroxide nanoparticles growth and metal adsorption/structural incorporation. In *Adsorption of Metals By Geomedia II*: *Variables, Mechanisms, and Model Applications*, Barnett, M. (Ed.), Elsevier Academic Press, 478.

Lanson B., Drits V. A., Silvester A., Manceau A. (2000) Structure of H-exchanged hexagonal birnessite and its mechanism of formation from Na-rich monoclinic buserite at low pH. *Am. Mineral*. **85**, 826–838.

Lee E. J. H., Ribeiro C., Longo E. and Leite E. R. (2005) Oriented Attachment: An Effective Mechanism in the Formation of Anisotropic Nanocrystals. *J. Phys. Chem. B.* **109**, 20842-20846.

Ligane J. J and Karplus R. (1946) New method for Determination of Manganese. *Ind. Eng. Chem. Anal*, Ed **18**, 191-194.

Liu L., Feng Q., Yanagisawa K., Bignall G., Hashida T. (2002) Lithiation reactions of Zn- and Li-birnessites in non-aqueous solutions and their stabilities. *J. Mater. Sci*. **37**, 1315–1320.

Liu Z. H., Kang L., Ooi K., Yoji M. and Feng Q. (2005) Studies on the formation of todorokite-type manganese oxide with different crystalline birnessites by Mg2+-templating reaction. *J. Colloid. Interf. Sci*. **285**, 239–246.

Livi K. J. T., Lafferty B., Zhu M., Zhang S., Gaillot A C., Sparks D. L. (2011) Electron Energy-Loss safe-dose limits for manganese valence measurements in environmentally relevant manganese oxides. *Environ. Sci. Technol.* **46**, 970-976.

Luo J., Zhang Q., Huang A., Giraldo O. and Suib S. L. (1999) Double-aging method for preparation of stabilized Na-buserite and transformations to todorokites incorporated with various metals. *Inorg. Chem*. **38**, 6106–6113.

Malinger K. A., Laubernds K., Son Y. C., Suib S. L. (2004) Effects of Microwave

Processing on Chemical, Physical, and Catalytic Properties of Todorokite-Type Manganese Oxides. *Chem. Mater.* **16**, 4296-4303.

Manceau A. and Combes J. M. (1988) Structure of Mn and Fe oxyhydroxides – a topological approach by EXAFS. *Phys. Chem. Min*. **15**, 283–295.

Manceau A., Drits V.A., Silvester E., Bartoli C. and Lanson B. (1997) Structural mechanism of Co^{2+} oxidation by the phyllomanganate buserite. *Am. Min*. **82**, 1150–1175.

Manceau A., Marcus M. A. and Tamura N. (2002) Quantitative speciation of heavy metals in soils and sediments by synchrotron X-ray techniques. In *Rev. Min. Geochem*. **49**, 341–428.

Manceau A., Lanson M. and Geoffroy N. (2007a) Natural speciation of Ni, Zn, Ba and As in ferromanganese coatings on quartz using X-ray fluorescence, absorption and diffraction. *Geochim. Cosmochim. Acta* **71**, 95–128.

McKenzie R. M. (1989) Manganese oxides and hydroxides: In *Minerals in Soil Environments*, J. B. Dixon and S. B.Weed, eds., Soil Science Society of America. Madison Wisconsin.

McKeown D. A. and Post J. E. (2001) Characterization of manganese oxide rock mineralogy in rock varnish and dendrites using X-ray absorption spectroscopy. *Am. Mineral.* **86**, 701–713.

Shen Y. F., Zerger R. P., DeGuzman R. N., Suib S. L., McCurdy L., Potter D. I. and O'Young C. L. (1993) Manganese oxide octahedral molecular sieves: preparation, characterization and application. *Science* **260**, 511–515.

Peacock C. L. and Sherman D. M. (2007a) Sorption of Ni by birnessite: equilibrium controls on Ni in seawater. *Chem. Geol*. **238**, 94–106

Peacock C. L. and Sherman D. M. (2007b) The crystal chemistry of Ni in marine ferro-manganese crusts and nodules. *Am Mineral*. **92**, 1087-1097.

Peacock C. L. (2009) Physiochemical controls on the crystal chemistry of Ni in birnessite: genetic implications for ferromanganese precipitates. *Geochim. Cosmochim. Acta* **73**, 3568–3578.

Peacock C. L. and Moon E. M. (2012) Oxidative scavenging of thallium by birnessite: Explanation for thallium enrichment and stable isotope fractionation in marine ferromanganese precipitates. *Geochim. Cosmochim. Acta* **84**, 297-313.

Peña J., Kwon K. D., Refson K., Bargar J. R. and Sposito G. (2010) Mechanisms of

Ni sorption by bacteriogenic birnessite. *Geochim. Cosmochim. Acta* **74,** 3076-3089.

Penn R. L. and Banfield J. F. (1998a) Imperfect Orientated Attachment: Dislocation Generation in Defect-Free Nanocrystals. *Science* **281**, 969-971.

Penn R. L. and Banfield J. F. (1998b) Orientated attachment and growth, twinning, polytypism, and formation of metastable phases: Insights from nanocrystalline TiO_2. *Am Mineral.* **83**, 1077-1082.

Penn R. L. and Banfield J. F. (1999) Morphology development and crystal growth in nanocrystalline aggregates under hydrothermal conditions: Insights from titania. *Geochim. Cosmochim. Acta* **63**, 1549-1557.

Penn R. L., Oskam G., Strathmann T. J., Searson P. C., Stone A. T., Veblen D. R (2001) Epitaxial assembly in aged colloids. *J. Phys. Chem. B*. **105**, 2177-2182.

Portehault D., Cassaignon S., Baudrin E. and Jolivet J. P. (2007) Morphology Control of Cryptomelane Type MnO_2 Nanowires by Soft Chemistry. Growth Mechanisms in Aqueous Medium. *Chem Mater*. **19**, 540-5417.

Post J. E. and Bish D. L. (1988) Rietveld refinement of the todorokite structure. *Am. Mineral.* **73**, 861–869.

Post J. E. and Veblen D. R. (1990) Crystal structure determinations of synthetic sodium, magnesium, and potassium birnessite using TEM and the Rietveld method. *Am. Mineral*. **75**, 477-489.

Post J. E. (1999) Manganese oxide minerals: crystal structures and economic and environmental significance. *Proc. Natl. Acad. Sci. U.S.A.* **96**, 3447–3454.

Post, J. E., Heaney, P. J. and Hanson, J. (2003) Real-time synchrotron X-ray powder diffraction studies of the structure and dehydration of todorokite. *Am. Mineral*. **88**, 142-150.

Ravel B. and Newville M. (2005) ATHENA, ARTEMIS, HEPHAESTUS: Data analysis for X-ray absorption spectroscopy using IFEFFIT. *J. Synchrotron Radiat.* **12**, 537-541

Saratovsky I., Wightman P. G., Pasten P. A., Gaillard J. F. and Poeppelmeier K. R. (2006) Manganese oxides: parallels between abiotic and biotic structures. *J. Am. Chem. Soc*. **128**, 11188–11198.

Shen Y. F., Zerger R. P., DeGuzman R. N., Suib S. L., McCurdy L., Potter D. I. and

Silvester E., Manceau A. and Drits V. A. (1997) Structure of synthetic monoclinic Na-rich birnessite and hexagonal birnessite; II, Results from chemical studies and EXAFS spectroscopy. *Am Mineral*. **82**, 962-978.

Sherman D. M. and Peacock C. L. (2010) Surface complexation of Cu on birnessite (δ-MnO2): controls on Cu in the deep ocean. *Geochim. Cosmochim. Acta* **74**, 6721–6730.

Siegel M. D. and Turner S. (1983) Crystalline todorokite associated with biogenic debris in manganese nodules. *Science* **219**, 172-174.

Silvester E. J., Manceau A. and Drits V. A. (1997) The structure of synthetic monoclinic Na-rich birnessite and hexagonal birnessite. II. Results from chemical studies and EXAFS spectroscopy. *Am. Mineral.* **82**, 962-978.

Spiro T. G., Barger, J. R., Sposito, G., Tebo, B. M. (2010) Bacteriogenic manganese oxides. *Acc. Chem. Res*. **43**, 2-9.

Takematsu N., Sato Y. and Okabe S. (1984) The formation of todorokite and birnessite in sea water pumped from underground. *Geochim. Cosmochim. Acta* **48**, 1099–1106

Tebo B. M., Johnson H. A., McCarthy J. K., Templeton A. S. (2005) Geomicrobiology of manganese (II) oxidation. *Trends Microbiol*. **13,** 421-428.

Tenderholt A., Hedman, B. and Hodgson K. O. (2007) PySpline: A modern, cross-platform program for the processing of raw averaged XAS edge and EXAFS data. *AIP Conf. Proc. (XAFS13)* **882,** 105-107.

Tian Z. H., Yin Y. G., Suib S. L. (1997) Effect of Mg2+ Ions on the Formation of Todorokite Type Manganese Oxide Octahedral Molecular Sieves. *Chem. Mater*. **9**, 1126-1133.

Toner B., Manceau A., Webb S.M. and Sposito G. (2006) Zinc sorption to biogenic hexagonal-birnessite particles within a hydrated bacterial biofilm. *Geochim. Cosmochim. Acta* **70**, 27–43.

Turner S., Siegel M. D., Buseck P. R. (1982) Structural features of todorokite intergrowths in manganese nodules. *Nature* **296**, 841-842.

Usui A. (1979) Nickel and copper accumulation as essential elements in 10 Å manganite of deep-sea manganese nodules. *Nature* **279,** 411-413.

Usui A., Bau M. and Yamazaki T. (1997) Manganese microchimneys buried in the Central Pacific pelagic sediments: evidence of intraplate water circulation? *Mar. Geol*. **141**, 269–285.

Usui A. and Terashima S. (1997) Deposition of Hydrogenetic and Hydrothermal Manganese Minerals in the Ogasawara (Bonin) Arc Area, Northwest Pacific. *Mar. Georesour. Geotech*. **15**, 127-154.

Van Driessche A. E. S., Benning L. G., Rodriguez-Blanco J. D., Ossorio M., Bots P., Garcia-Ruiz J.M. (2012) The role and implications of bassenite as a stable precursor phase to gypsum precipitation. *Science* **336**, 69-72.

Vileno E., Ma Y., Zhou H., Suib S. L. (1998) Facile synthesis of synthetic todorokite OMS-1), co-precipitation reactions in the presence of a microwave field. *Micropor. Mesopor. Mat.* **70,** 3-15.

Villalobos M., Toner B., Bargar J. and Sposito G. (2003) Characterization of the manganese oxide produced by Pseudomonas putida strain MnB1. *Geochim. Cosmochim*. Acta **67**, 2649–2662.

Villalobos M., Lanson B., Manceau A., Toner B. and Sposito G. (2006) Structural model for the biogenic Mn oxide produced by Pseudomonas putida. *Am. Mineral*. **91**, 489–502.

Waychunas G. A, Kim C. S and Banfield J. F. (2005) Nanoparticulate iron oxide minerals in soils and sediments: unique properties and contaminant scavenging mechanisms. *J. Nanopart. Res*. **7**, 409-433.

Webb S. M., Tebo B. M. and Bargar J. R. (2005a) Structural characterization of biogenic manganese oxides produced in seawater by the marine Bacillus sp. strain SG-1. *Am. Mineral*. **90**, 1342–1357.

Webb S. M., Dick G. J., Bargar J. R. and Tebo B .M. (2005b) Evidence for the presence of Mn(III) intermediates in the bacterial oxidation of Mn(II). *Proc. Natl. Acad. Sci. U.S.A.* **102**, 6. 5558-5563.

Xu H., Chen T., Konishi H. (2010) HRTEM investigation of trilling todorokite and nano-phase Mn-oxides in manganese dendrites. *Am. Mineral*. **95**, 556-562.

Zhang J., Huang F. and Lin Z. (2009) Progress of nanocrystalline growth kinetics based on orientated attachment. *Nanoscale.* **2**, 18-34.

1053 **TABLES**

1054

1055 **TABLE 1:** Specific surface area of the solid products and pH of the reflux solution
1056 for the c-disordered birnessite precursor, Mg-phyllomanganate intermediate and all
1057 subsequent reflux products.

1058

Sample	Surface Area (m^2/g)[a]	Reflux Soln. pH[b]
C-disordered birnessite	103.7	N/A
Mg-phyllomanganate	104.9	N/A
3hr-Reflux	78.82	4.80
6hr-Reflux	82.47	4.85
9hr-Reflux	76.24	4.85
12hr-Reflux	75.36	4.86
24hr-Reflux	94.81	4.89
48hr-Reflux	69.95	5.10
72hr-Reflux	65.82	5.51

1059 [a]All surface area measurements are ±5%. [b]All pH measurements are ±0.05 pH units.

1060

1061 **FIGURE CAPTIONS**

1062

1063 **FIGURE 1:** X-ray diffraction patterns: a) c-disordered birnessite precursor and Mg-
1064 exchanged phyllomanganate intermediate and b) Mg-exchanged phyllomanganate
1065 intermediate (repeated from Fig. 1a) and all subsequent reflux products.
1066 Characteristic X-ray diffraction peaks are labeled for our c-disordered birnessite (B),
1067 Mg-exchanged phyllomanganate intermediate (MgI) and todorokite product (T)
1068 (based on Drits et al., 1997 for turbostratic birnessite, JCPDS-32-1128 for buserite
1069 and JCPDS-38-475 for todorokite).

1070

1071 **FIGURE 2:** Fourier transform infrared powder absorption spectra of c-disordered
1072 birnessite precursor, Mg-exchanged phyllomanganate intermediate, and reflux
1073 products at 6 hr, 12 hr, 24 hr and 72 hr reflux. Dashed line shows characteristic broad
1074 peak at ~760 cm^{-1} that is typically assigned to an asymmetrical Mn-O stretching
1075 vibration, corresponding to corner-sharing MnO_6 octahedra.

1076

1077 **FIGURE 3:** Scanning electron micrographs: a) c-disordered birnessite precursor, and
1078 reflux products at b) 6 hr reflux, c-d) 72 hr reflux.

1079

1080 **FIGURE 4:** Transmission electron micrographs of: (a - b) c-disordered birnessite
1081 precursor and (c – d) Mg-exchanged phyllomanganate intermediate with b) and d)
1082 highlighting the repetition of the [001] lattice planes, (e) reflux product at 1.5 hr
1083 showing rumpling and distortion of the phyllomanganate layers, (f) reflux product at 6
1084 hr showing primary particles of todorokite (white outlines) elongated longitudinally
1085 along [010] and aggregating laterally across [100] to form todorokite laths, (g) reflux
1086 product at 48 hr showing todorokite laths ~ 50-100 nm wide (black lines highlight
1087 primary particle aggregation), (h) reflux product at 72 hr showing todorokite laths ~
1088 100-150 nm wide (black lines highlight primary particle aggregation), (i) reflux
1089 product at 24 hr showing crystalline laths of todorokite elongated along [010] with
1090 laths overlapping and aligned at 120°, (j) reflux product at 72 hr showing todorokite
1091 with a plate-like morphology with plates comprised of aligned overlapping laths, also
1092 showing in the enlarged area a number of linear dislocations along the direction of
1093 tunnel growth (highlighted with white lines), (k) reflux product at 72 hr showing
1094 heterogeneous todorokite tunnel dimensions.

1095

1096 **FIGURE 5:** Specific surface area of the solid products and pH of the reflux solution
1097 for the reflux time series. The first surface area measurement shown on the plot is the
1098 Mg-exchanged phyllomanganate intermediate at 0 hr aging time; pH measurements
1099 start at 3 hr reflux. For exact values see Table 1.

1100

1101 **FIGURE 6:** Mn K-edge EXAFS for Mn oxide reference compounds and our c-
1102 disordered birnessite precursor, Mg-exchanged phyllomanganate intermediate and
1103 reflux products at 20 min, 1.5 hr and 3hr reflux. Vertical dashed lines mark the
1104 positions of the *k*-space indicator regions at ~6.7, 8 and 9.2 $Å^{-1}$.

1105

1106 **FIGURE 7:** Simplified model for the growth of todorokite: a) primary todorokite
1107 particles, b) oriented attachment of primary todorokite particles to form larger and
1108 more stable secondary todorokite laths, and c) further aggregation of todorokite laths
1109 to form todorokite with a plate-like morphology.

Atkins et al: Figure 1 (two columns wide)

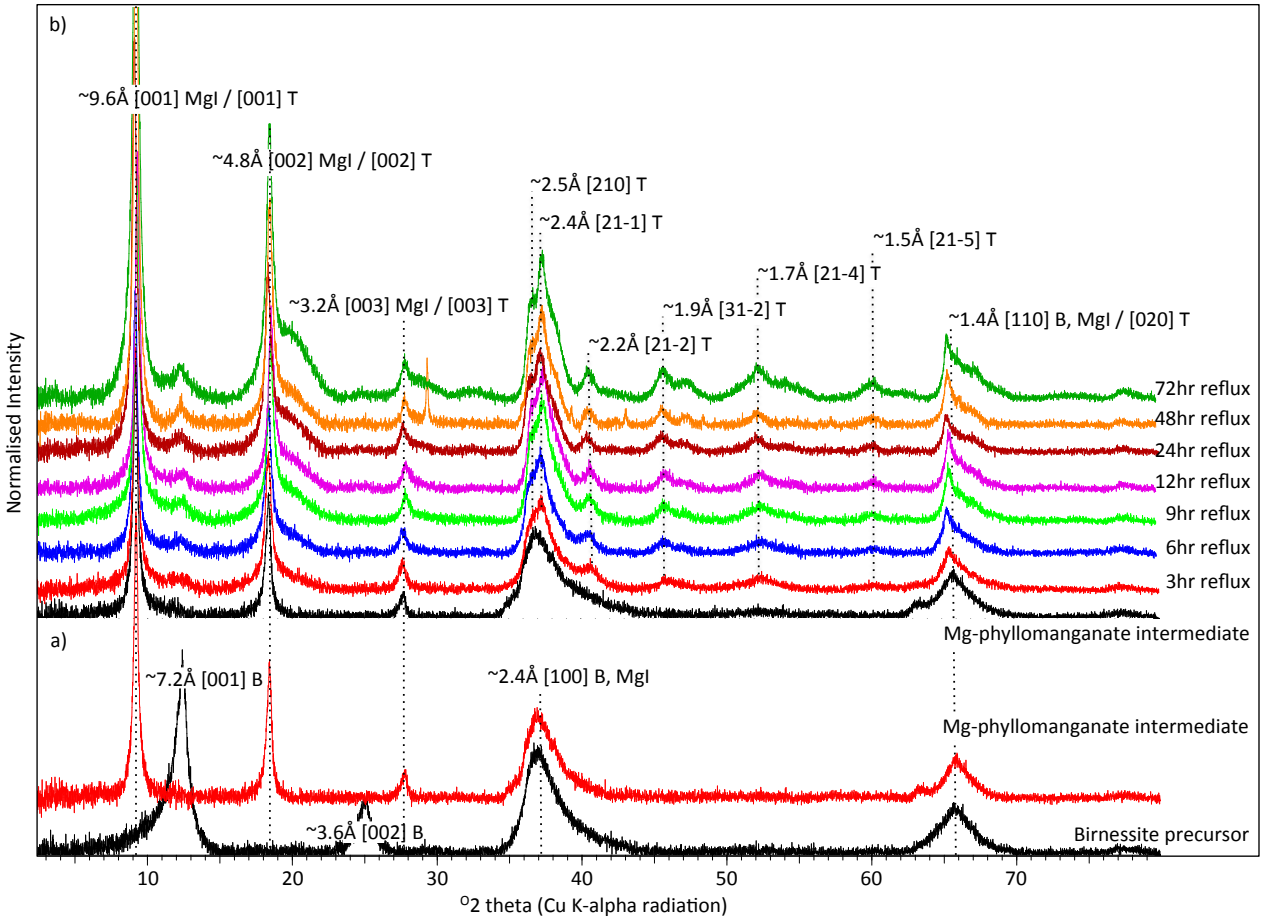

1110

Atkins et al: Figure 2 (one column wide)

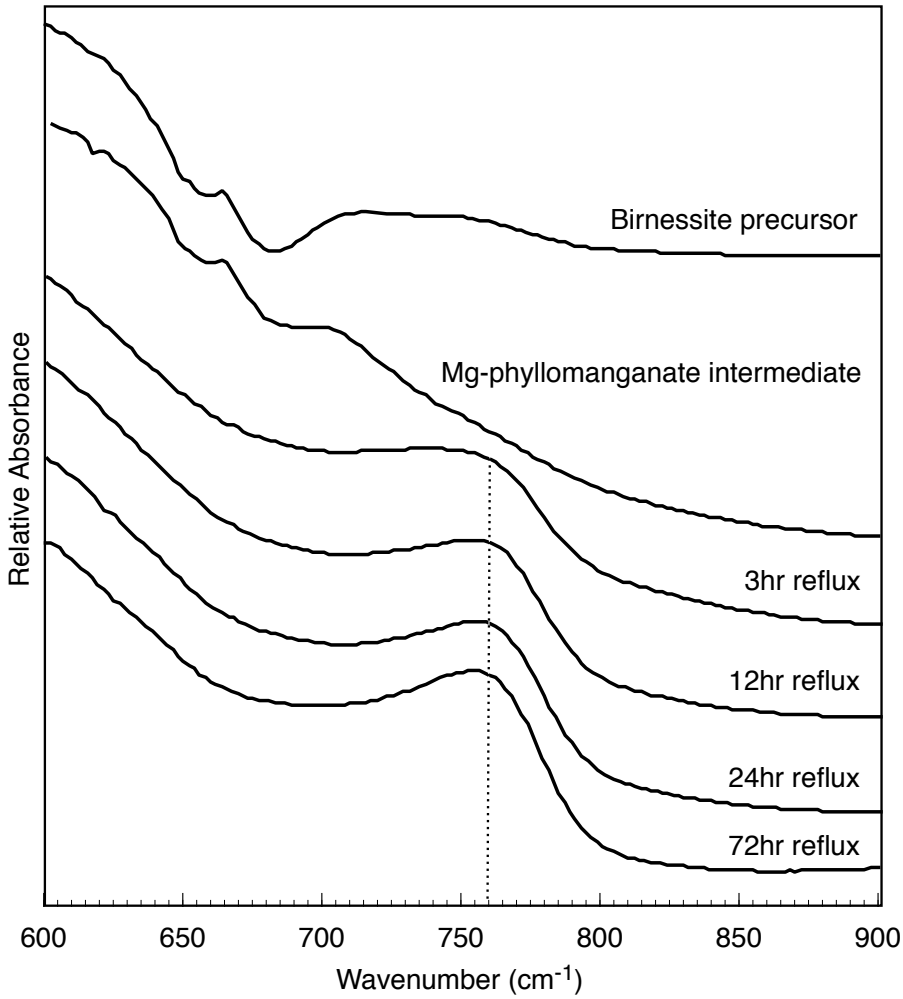

1111

Atkins et al: Figure 3 (two columns wide)

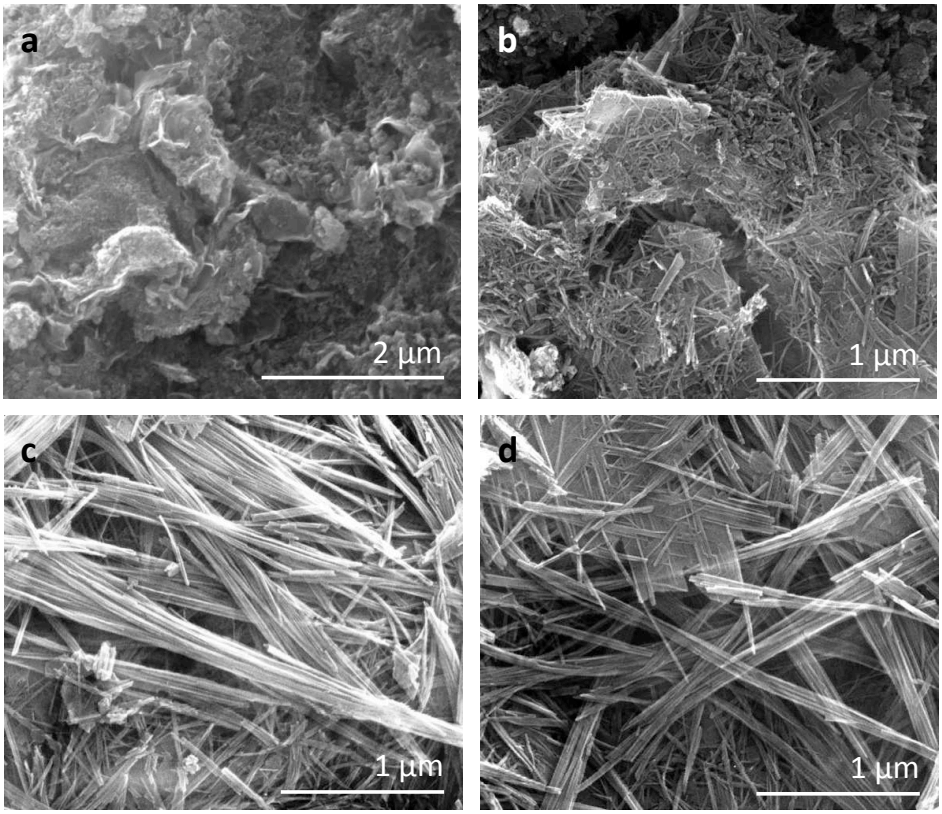

1112

Atkins et al: Figure 4 a-f (two columns wide)

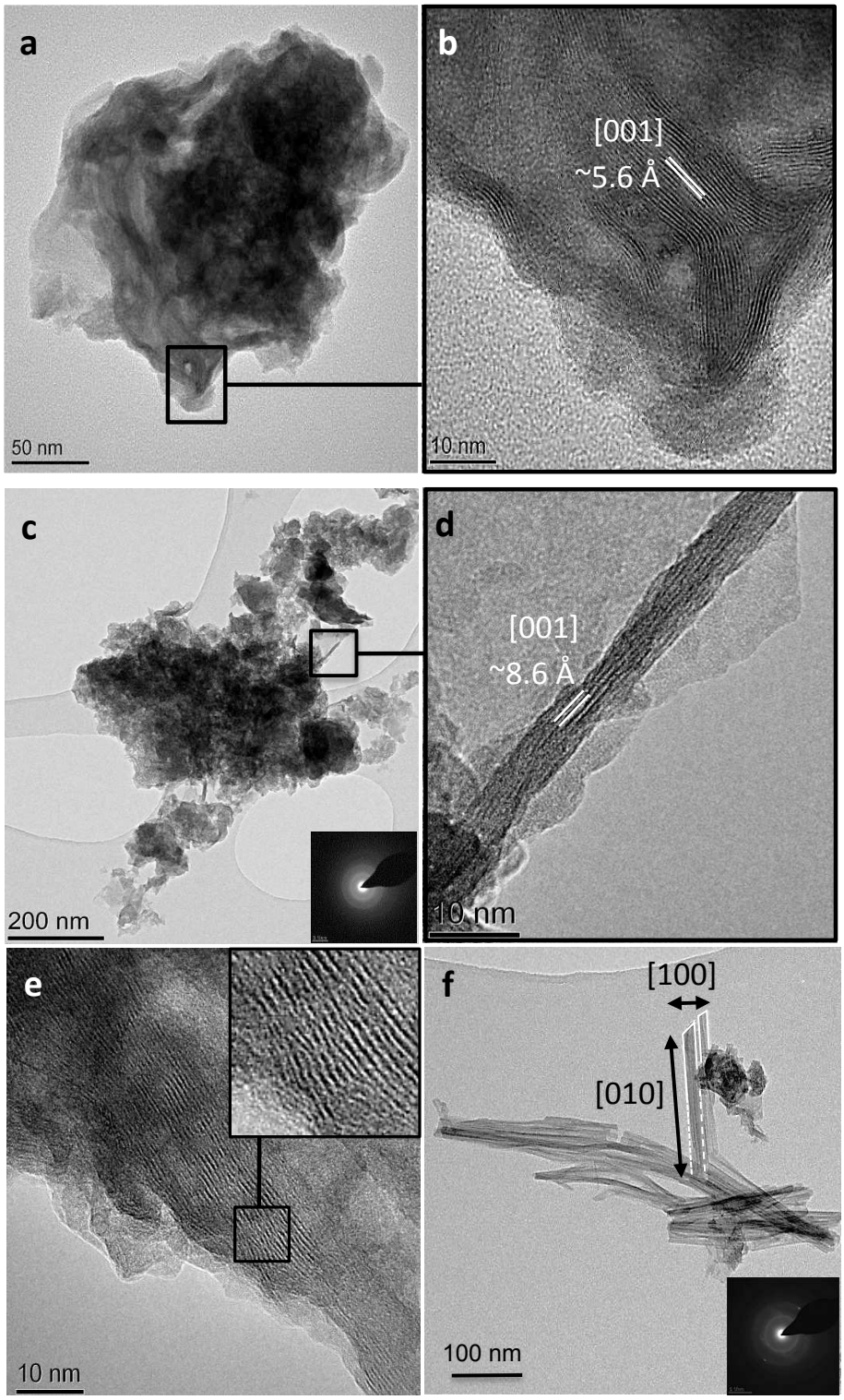

1113

Atkins et al: Figure 4 g-k (two columns wide)

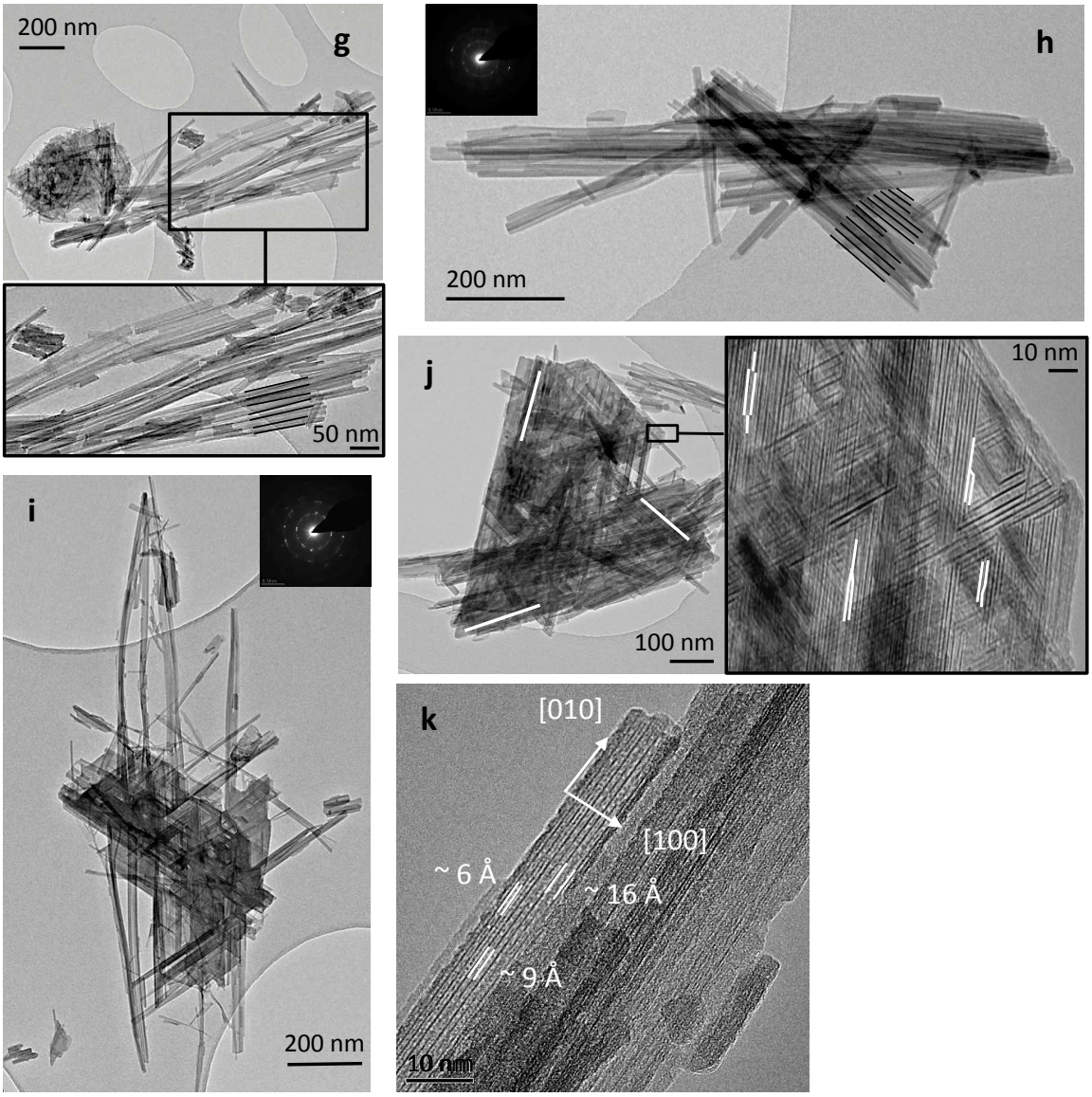

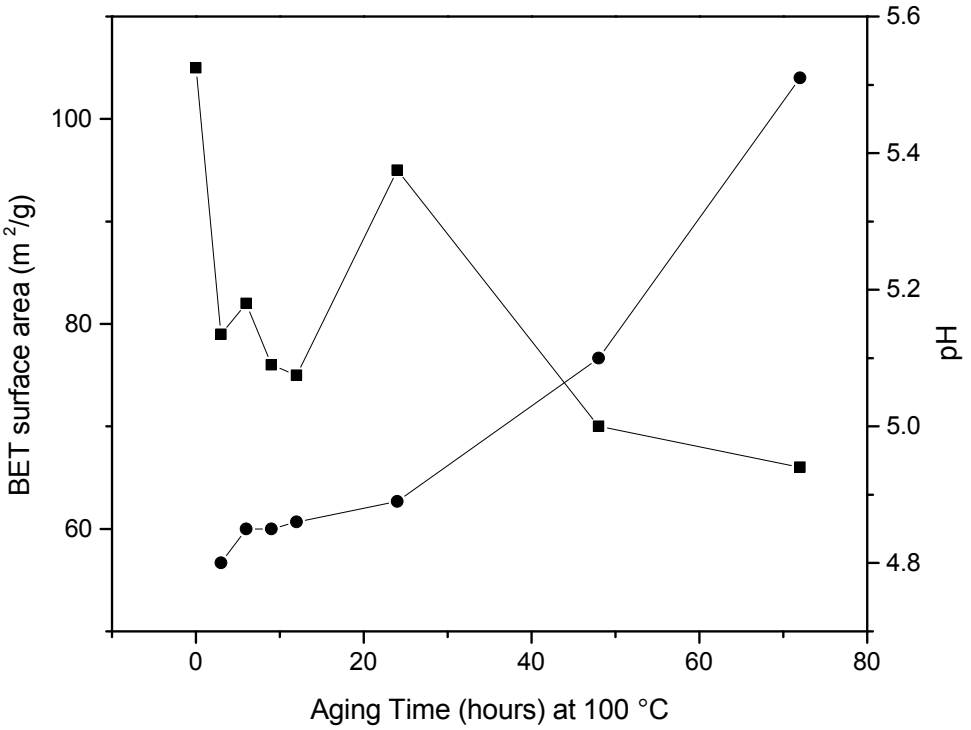
BET surface area (m 2/g)
100
80
60
pH
5.6
5.4
5.2
5.0
4.8
0
20
40
60
80
Aging Time (hours) at 100 °C

1116

Atkins et al: Figure 6 (two columns wide)

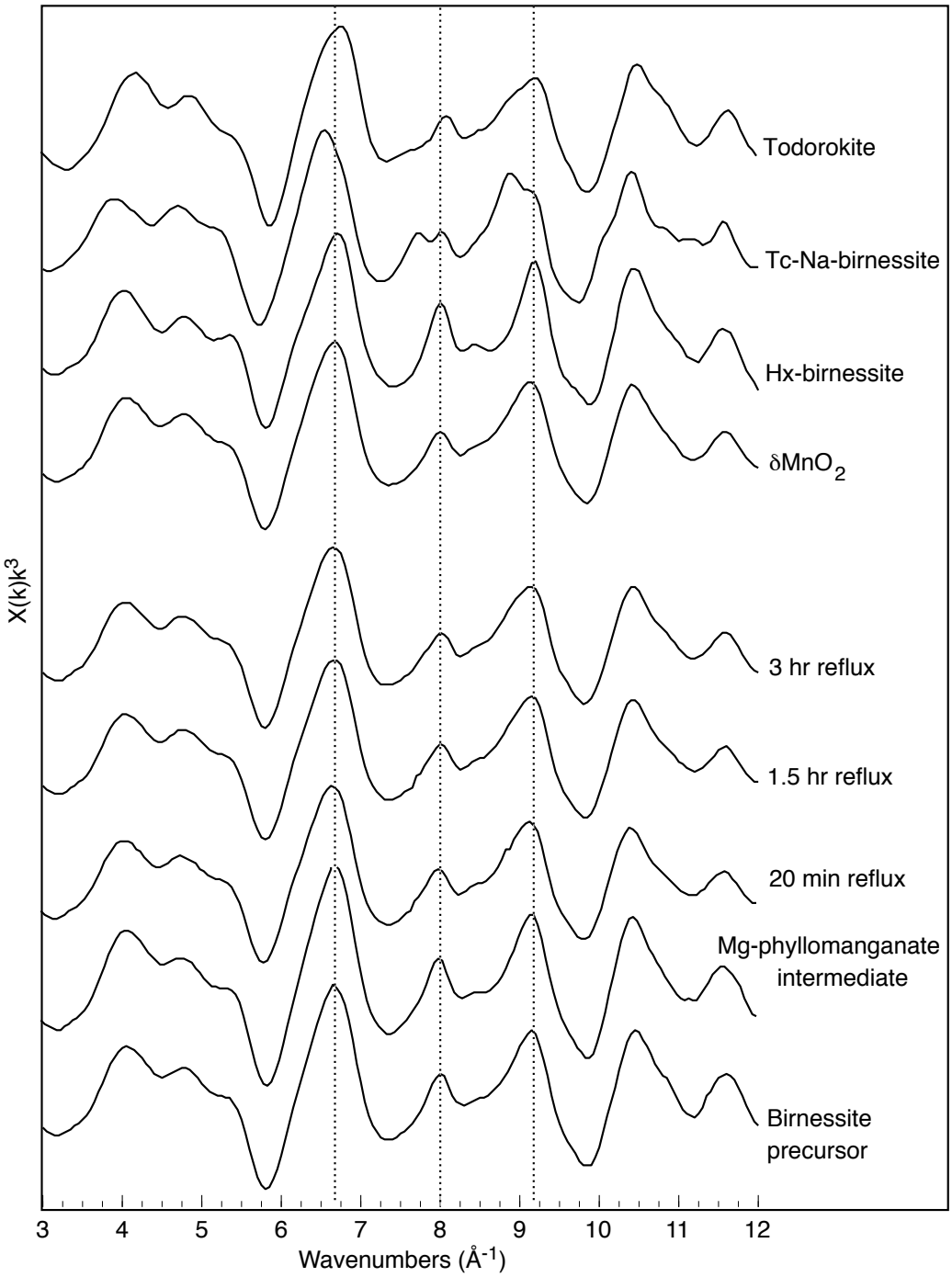

1117

Atkins et al; Figure 7 (one column)

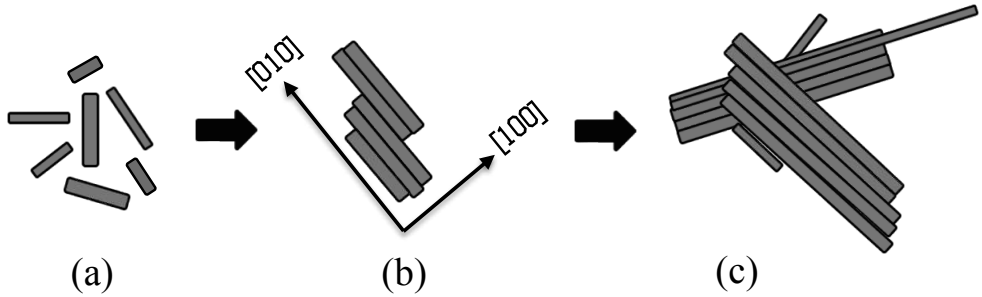

1118